Investigation of a
Collapsed Cone Superposition Algorithm
for dosimetry in brachytherapy

Freja Alpsten

freja@alpsten.com

August 19, 2021

Defended on the 24th of June 2021

Master of Science Thesis in Medical Radiation Physics
Department of Physics, Stockholm University

Supervised by
Åsa Carlsson Tedgren
Department of
Medical Radiation Physics and Nuclear Medicine,
Radiotherapy Physics and Engineering,
at the Karolinska University Hospital
&
Adjunct senior lecturer & Ass. prof.
at Linköping University

Abstract

Background & Purpose: The current standard dosimetry in brachytherapy treatment planning, the TG-43 formalism, ignore the presence of non-water media and finite patient dimensions [1, 2]. This can cause clinically relevant errors in dose estimates [3]. To overcome the limitations of the TG-43 formalism, Model-Based Dose Calculation Algorithms (MBDCAs) have evolved. One of the commercial available MBDCAs is the Advanced Collapsed cone Engine (ACE) by Elekta [4]. In ACE, the total dose is divided into three components, the primary, the first-scattered and the multiple-scattered dose, where the two last mentioned are calculated by the means of the Collapsed Cone Algorithm [5, 6].

In this study the performance of ACE has been investigated. The study has been divided into 2 parts, where the aim of part 1 was to analyze the relationship between the so called discretization artifacts, caused by the collapsed cone approximation, and the number of dwell positions. The severeness of the artifact is thought to decrease as the number of dwell positions are increased [7]. The second part focus on ACE's behavior in cortical bone, with the aim to form a hypothesis (explanation and solution) to the previously observed dose underestimation of the dose to bone made by ACE [7–9].

Materials and Methods: The generic ^{192}Ir source, the Oncentra Brachy (OcB) treatment planning system (TPS) and the Monte Carlo (MC) platform ALGEBRA have been utilized. In the first part of the study, six source configurations, all with a different number of dwell positions, were created and placed in the center of large water phantoms, i.e. under TG-43 conditions in which the TG-43 formalism can be assumed to yield a high accuracy of the estimated dose. The accuracy of ACE has been judged by its' deviation from TG-43.

In the second part of the study, a cubic source configuration, of 27 dwell positions, was positioned at the center of a cubic water phantom. Three cases where constructed, with a small cortical bone heterogeneity positioned at different distances from the source configuration. The ACE calculated dose distribution has been divided into its' three constituents. The accuracy of ACE and TG-43 has been judged by its' deviation from MC.

Results: Part 1 showed that increasing the number of dwell positions does not guarantee an improved accuracy of ACE. Local dose difference ratios of > 2%, caused by the artifacts, were mainly located outside the 5% isodose line. A general dose underestimation was observed in ACE, with an increased magnitude as the dose level decreased. The majority of local dose difference ratios below -4% were found where the multi-resolution voxelization grid of ACE has a voxel size of $\geq 2^3$ mm^3, that is at a distance of ≥ 8 cm from the closest dwell position when using the ACE standard accuracy level.

In part 2, ACE underestimated the dose to cortical bone, with an increased magnitude as the bone was positioned farther away from the source configuration. The TG-43 formalism gave slightly better estimates of the mean dose to bone than ACE, especially at higher dose levels. For a mean dose to the cortical bone heterogeneity equal to 45% of the prescribed dose, TG-43 and ACE underestimated the mean dose with 1% and 4%, respectively. The estimated mean dose to a volume located directly behind the heterogeneity agreed within 1% between ACE and MC. However, an increased amount of positive local dose difference ratios were observed in this volume.

Conclusions: Increasing the number of dwell positions cause a "blurring" effect of the artifact (see Ma et al. [7]), but may also increase the fluence gradient. In such situations the severeness of the artifact may not be improved. In patient cases the dwell positions are usually added in a more random manner which may favor the "blurring effect".

The underestimations observed in ACE are thought to be caused by both the multiple-resolution voxelization grid of ACE and the relationship between the dimensions of the phantom in which the multiple-scattered kernel has been generated and the current calculation volume [10].

ACE was unsuccessful to predict the dose to cortical bone, and should hence be used with caution when cortical bone is an organ at risk, as long as the problem remains. The results indicates that the error in ACE is located in the scatter dose calculations and that the heterogeneity cause ACE to displace the dose.

The error is thought to be located in the multiple-scattered dose component, which was also shown by Terribilni et al. [11]. A hypothesis is that the problem is caused by the neglected effect of media dependent absorption coefficients in the multiple-scattered dose calculation. A suggested solution, left to be proven, is to use effective attenuation scaling factors [12].

Acknowledgements

I would like to express my gratitude to all who have helped me throughout this project.

Contents

List of abbreviations & nomenclature

Abbreviations

1D   One dimension

2D   Two dimensions

3D   Three dimensions

AAPM   American Association of Physics in Medicine

ACE   Advanced Collapsed cone Engine

CPE   Charged Particle Equilibrium

CT   Computational Tomography

DICOM   Digital Imaging and Communications in Medicine

DP   Dwell Position

EBT   External Beam Therapy

HDR   High Dose-Rate

MBDCA   Model Based Dose Calculation Algorithm

MC   Monte Carlo

OAR   Organ At Risk

OcB   Oncentra Brachy

ROI   Region Of Interest

TG-186   AAPM Task Group 186

TG-43   AAPM Task Group 43

TPS   Treatment Planning system

Nomenclature

S scerma: SCattered Energy Released per unit MAss

K kerma: Kinetic Energy Released per unit MAss

K_c	collision kerma
^{192}Ir	Iridium 192
$D_{\textbf{prim}}$	Primary dose
$D_{\textbf{sc}}$	Scattered dose
$D_{\textbf{1sc}}$	First-scattered dose
$D_{\textbf{msc}}$	Multiple-scattered dose
$\overline{E}$	Weighted average energy of photon spectrum
μ	Linear attenuation coefficient
$\mu_{\textbf{en}}$	Linear absorption coefficient
$\tilde{h}_{1\text{sc}}$	First-scattered dose kernel/energy deposition kernel
$\tilde{h}_{\Psi,1\text{sc}}$	First-scattered energy fluence kernel
$\tilde{H}_{\text{msc}}$	Multiple-scattered dose kernel/energy deposition kernel
$\tilde{H}_{\Psi,\text{msc}}$	Multiple-scattered energy fluence kernel
R	Radiant energy
$\hat{R}$	Radiant energy fluence
$D_{\textbf{per}}$	Prescribed dose
$D^{\textbf{TG43}}(\mathbf{r})$	Dose distribution as calculated with the TG-formalism
$D^{\textbf{ACE}}(\mathbf{r})$	Dose distribution as calculated with ACE
$D^{\textbf{MC}}(\mathbf{r})$	Dose distribution as calculated with MC
$\Delta D^{x}_{\textbf{ref}}$	Local dose difference ratio of $D^{x}(\mathbf{r})$ with $D^{\text{ref}}(\mathbf{r})$ as the reference
$D_{\textbf{w,w}}$	Dose to water in water
$D_{\textbf{w,m}}$	Dose to water in media
$D_{\textbf{m,m}}$	Dose to media in media

1. Introduction

Brachytherapy, a form of radiotherapy, is widely used as a treatment to various cancer forms, there among prostate-, cervix-, and head and neck cancers [13]. The treatment is either used as a single treatment, in combination with external beam therapy (EBT), or as a part of an extensive oncological care program, involving e.g. chemotherapy, hormone therapy, surgery etc. The procedure is performed by placing sealed photon emitting sources[1] in or very close to the target, enabling high radiation doses to be delivered per fraction, while limiting exposure of surrounding tissues and maintaining acceptable dose levels to organs at risk (OAR) [13]. This as the dose distribution around a source exhibit steep gradients caused by the inverse-square law, and geometrical uncertainties are minimized as the source moves with the target [13, 15].

Dosimetry algorithms for treatment planning needs to be fast and accurate to be of clinical use. Today, the standard way to perform treatment planning at the clinics are based on the recommendations and dose calculation formalism of the American Association of Physics in Medicine (AAPM) Task Group number 43 (TG-43) [1, 16–18]. The formalism relies on pre-calculated dose distributions around single sources in water. The final dose distribution in a treatment plan is obtained by superpositioning of single source dose distributions in accordance with the dwell positions relative location and dwell times. Dose calculations using the formalism is fast and, in most cases, yield good accuracy at clinically relevant dose levels. This is especially true for ^{192}Ir sources, the most common isotope in clinical use at the moment, which have a weighted average energy ($\overline{E}$) of approximately 400 keV [14]. However, the TG-43 formalism does not take heterogeneities, inter-seed attenuation or finite patient dimensions into consideration[2] [19]. Significant errors ($\geq 5\%$) in estimated dose parameters may occur when utilizing the formalism in situations where attenuation and scattering conditions deviate considerably from the all water case [3]. Categories of clinical applications where the TG-43 formalism fails to give acceptable accuracy has been reviewed Beaulieu et al. ([19]) and by Rivard et al. ([3]), and some examples are presented in section 2.1.2 of this thesis.

To achieve acceptable accuracy where the TG-43 formalism fails, Model-Based Dosimetry Calculation Algorithms (MBDCAs) have emerged. Among the MBDCAs of current interest is Monte Carlo (MC) simulations, grid-based Boltzmann solvers, and the collapsed cone superposition algorithm [19]. The first mentioned, MC, offers the highest accuracy but to a cost of speed that is yet too high for any approved MC code to be of clinical use [2].

The last mentioned MBDCA, the collapsed cone superpositioning algorithm, was first introduced by Ahnesjö for dosimetry in EBT and has been adopted for scattered-dose calculations in brachytherapy by Carlsson Tedgren and Ahnesjö [5, 6, 15]. It has been made commercially available for dosimetry in ^{192}Ir treatments, under the name Advanced Collapsed cone Engine (ACE) in the Oncentra Brachy (OcB) treatment planning system (TPS) by Elekta [4].

As the name reveals, the collapsed cone superpositioning algorithm is a kernel superpo-

---

[1]The radioactive isotopes utilized may not only emit photons, but the sources encapsulation are often designed so that electrons are prevented from leaving the source core. Sources emitting other particles such as beta particles also exist, but photon emitting sources is the most common [14]

[2]One-dimensional heterogeneity corrections, based on the "effective path length", exists but these are only appropriate for attenuation corrections of the primary photon spectra [19].

sition/convolution method, in which MC derived dose kernels are superimposed with the distribution of Scattered Energy Released per unit MAss (scerma). In brachytherapy the algorithm is used for scattered dose (D_{sc}) calculations as the primary dose, D_{prim}, can be determined by ray tracing [2]. Here, D_{prim} and D_{1sc} are the dose liberated by charged secondaries following primary photon interactions and scattered photon interactions, respectively.

In the algorithm the kernels are discretized, or collapsed, into cones and the energy transport, i.e. attenuation and deposition, is restricted to solely the cone axes [15]. To improve computational efficiency, parallel cone axes from different voxels are arranged to overlap with each other, forming a lattice of transport lines over the entire Cartesian grid in which the dose is to be calculated [15]. This discretization is called "The collapsed cone approximation". In contrast to EBT, brachytherapy beams are highly divergent with steep fluence gradients, factors that are challenging for the algorithm [15]. Hence, the collapsed cone approximation becomes more critical in brachytherapy than in EBT and give rise to discretization artifacts.

The aim of this study was to investigate the commercially available collapsed cone dose engine ACE, using an ^{192}Ir source. The study has been divided into two parts, where the first part of the study focus on the artifacts dependence on the number of dwell positions. The severeness of the artifact is expected to decrease in multiple-source configurations as a result of decreased fluence gradients and a blurring effect when artifacts from different dwell positions superimpose [7, 20].

The second part of this study investigates ACE's performance in cortical bone. This as previous studies has shown that ACE tends to underestimate the dose to bone [7–9]. To correctly account for bone heterogeneities is necessary to make informed evaluations about the benefits and risks of a treatment plan where an OAR is positioned behind a bone heterogeneity, or where the bone itself is a major OAR. The latter is of special importance when treating head and neck cancers (with brachytherapy and/or EBT), such as oral tongue carcinoma, where long term side effects such as osteoradionecrosis has a significant risk of occurring [21]. It is also important to know the dose to bone when treating pediatric patients (especially rhabdomyosarcomas), as radiation of the bone at young age may also lead to growth retardation, leaving the children with long term side effects such as pain and psychosocial challenges [22, 23]. The goal of the study was to find a possible explanation to the reported behavior of ACE, and suggest solutions to be investigated in future studies.

2. Theory

2.1. The TG-43 formalism

The TG-43 dosimetry formalism was first introduced in 1995, in a dosimetry protocol by AAPM, to establish standardization of dose-calculation methodologies in brachytherapy [16]. In 2004 the AAPM Low Energy Brachytherapy source Dosimetry (LEBD) Working Group published an updated version of the TG-43 protocol (TG-43U1) [1, 17]. The recommendations and guidelines presented in the TG-43U1 report is in general also applicable to high energy (> 50 keV) source dosimetry, with some variances addressed by the AAPM High Energy Brachytherapy Dosimetry (HEBD) working group [18]. Below follows a brief introduction to the formalism and a discussion of its' limitations.

2.1.1. The TG-43 dose calculation algorithm

The TG-43 formalism utilize an effective parameterization of the dose-rate to water, which allows for the construction of compact source specific data tables, with a few values of the parameters at discrete locations. This by assuring adequate accuracy is kept when performing table interpolations. There are three parameters per source: the dose-rate constant (Λ), the radial dose function ($g(r)$), and the anisotropy function ($F(r, \theta)$). These parameters, given in the AAPM reports [1, 17, 18], have been derived from multiple published data sets, reporting either Monte Carlo or experimentally derived TG-43 dosimetry parameters, to form a single consensus data set per source [1].

The TG-43 formalism assumes the source to be cylindrical symmetric[3] and calculates the two dimensional (2D) dose-rate spatial distribution, $\dot{D}(r, \theta)$, from a single source in a large water phantom as,

$$\dot{D}(r, \theta) = S_k \Lambda \frac{G_L(r, \theta)}{G_L(r_0, \theta_0)} g_L(r) F(r, \theta), \tag{1}$$

where S_K is the air-kerma strength, $G_L(r, \theta)$ is the geometry function, r denotes the distance from the center of the active source to the point of interest and θ is the polar angle between this point and the source longitudinal axis [1]. The reference distance is denoted r_0 and equal 1 cm, and θ_0 is the reference angle which equals 90° and defines the transverse plane of the source [1]. Below follows a short description of equation 1 and its' parameters.

The air-kerma strength is defined as the air-kerma rate at a distance d, generated by photons of an energy exceeding δ, multiplied by d^2 [1],

$$S_K = \dot{K}_\delta(d) d^2. \tag{2}$$

It is defined "*in vacuo*", which means that experimental measurements in air has to be corrected for attenuation and scattering [1].

The product of S_K and Λ, where Λ is defined as [1],

$$\Lambda = \frac{\dot{D}(r_0, \theta_0)}{S_K}, \tag{3}$$

yields the absorbed dose-rate at the reference point $P(r_0, \theta_0)$, i.e. $\dot{D}(r_0, \theta_0)$. As the source is assumed to be cylindrical symmetric, the spatial dose distribution in the central axis plane ($\theta = \theta_0$) is one-dimensional and obtained by applying appropriate scatter-, attenuation- and geometry corrections to $\dot{D}(r_0, \theta_0)$.

As the steep dose gradients in brachytherapy are mainly caused by the inverse square-law, excluding the geometry correction from the tabulated parameters improve the accuracy of the dose-rate estimates when interpolations between discrete points in the data tables are performed [1]. Hence, an effective inverse square-law correction $G_L(r, \theta)/G_L(r_0, \theta_0)$ is applied separately to $\dot{D}(r_0, \theta_0)$. Simplistic approximations of $G_L(r, \theta)$ may be used as the important part lies in consistency, i.e. that the same form of $G_L(r, \theta)$ is used in equation 1 as was used in the derivation of $g_L(r)$ and $F(r, \theta)$ [1].

---

[3]The TG-43 protocol also includes a one dimensional (1D) formalism in which the source is approximated as an isotropic point source. This formalism will not be presented here. The subscript L on $G_L(r, \theta)$ and $g_L(r)$ is to state that the line approximation is used.

The radial dose function, $g_L(r)$ preforms the scatter- and attenuation corrections, and is defined as [1],

$$g_L(r) = \frac{\dot{D}(r, \theta_0)}{\dot{D}(r_0, \theta_0)} \frac{G_L(r_0, \theta_0)}{G_L(r, \theta_0)}. \tag{4}$$

To calculate the dose to any point $P(r, \theta)$, the use of the anisotropy function is necessary as most sources yield anisotropic dose distributions in the longitudinal plane. The anisotropy function is defined as [1],

$$F(r, \theta) = \frac{\dot{D}(r, \theta)}{\dot{D}(r, \theta_0)} \frac{G_L(r, \theta_0)}{G_L(r, \theta)}. \tag{5}$$

The dose-rate contribution from the source to a point of interest is calculated separately for each dwell position (alternatively each source in case of permanent implants) using equation 1. The final spatial dose distribution in a treatment plan is then obtained by summation of single source dose distributions according to their relative positions and dwell times [1].

2.1.2. Limitations in the TG-43 formalism

As explained above the TG-43 formalism calculates the dose distribution around a single source, centrally positioned in a large water phantom, and superimpose dose distributions from single sources [19]. The algorithm hence neglects the effects of (1) finite patient dimensions, (2) inter-seed attenuation, (3) applicator shielding, and (4) patient inhomogeneities [1, 3, 19]. These 4 limitations of the TG-43 formalism affects the ability of the formalism to accurately calculate the dose in some specific cases. A worst case scenario for respective limitation is presented below. Note that only a limited number of selectively chosen studies has been brought up in the following, as the purpose was not to evaluate the accuracy of the TG-43 formalism, but to highlight some situations where brachytherapy dosimetry may benefit from MBDCAs.

The effects of the first limitation, i.e. disregarding the patient's dimensions, may result in dose over-estimations in treatment plans where the target is anatomically shallow-seated. In brachytherapy of breast cancer, over-estimations in the range of 5-30% has been reported at points close to the tissue/air interface [24]. Pantelis et al. performed a study on dosimetry in brachytherapy breast treatments, using a patient-equivalent mathematical phantom [25]. Their result showed that the TG-43 formalism over-estimated the skin dose with up to 10% as compared to MC calculations, and hence, they concluded, among other things, that skin dose calculations, in breast treatments, using the TG-43 formalism should be thought of as an conservative approach [25].

The neglected effect of inter-seed attenuation is of most concern in permanent implants of low energy sources (< 50 keV), e.g. for treatments of prostate cancer. Underestimations of the CTV D_{90}[4] ranging from 1-5% has been reported in the literature (see the review by Kirisits et al. [24]) and errors exceeding 10% along the insert-needle direction may occur when utilizing the TG-43 formalism [3].

In gynecological treatments of the uterus, applicators with high-Z shields can be used to reduce the dose to the bladder and the rectum [3]. These shields can cause a dose reduction

---

[4]The definition of D_{90}: 90% of the CTV gets a dose of D_{90} or higher.

at the unshielded side of the applicator as the scatter-conditions are altered [24]. For a virtual monoenergetic point source of 60 keV, this dose reduction has been shown to be around 10 % at 1 cm from the source [2]. Neglecting applicator shielding and scattering may hence lead to errors in the estimated target dose.

The last mentioned limitation of the TG-43 formalism is the neglected effect of patient inhomegeneities. In a study by Anagnostopoulos et al. the presence of inhomogeneities in an ^{192}Ir High Dose-Rate (HDR) brachytherapy treatment of the upper thoracic oesophageal showed to alter the dose by $> \pm 10\%$ in OARs [26]. However, as brachytherapy dose distributions are characterized by steep gradients, the actual dose levels in the OARs were low (5-10% of the prescribed dose) and hence, the effect of inhomogeneities of no clinical relevance when brachytherapy is the single modality. Nonetheless, the effects could be of significance when brachytherapy is used as a boost to EBT [26].

2.2. The collapsed cone superposition algorithm in brachytherapy

In the following sections the underlying theory of the collapsed cone dose engine in brachytherapy will be explained. First, the "collapsed cone approximation" is introduced and its' effects on dosimetry in brachytherapy is discussed. Then the "successive-scattering kernel superposition" method, developed to reduce the effects of the approximation, will be described, followed by a brief explanation of kernel parameterization. Last, the recursive stepping approach and a kernel scaling method to account for heterogeneities are presented.

2.2.1. The collapsed cone approximation

The collapsed cone algorithm in brachytherapy is a method to perform convolution, or superposition, of scerma distributions with dose kernels to obtain the "scattered dose" D_{sc}. The convolution/superposition is performed with the use of the so called "collapsed cone approximation", which restricts the directions of which were scerma can be transported [5].
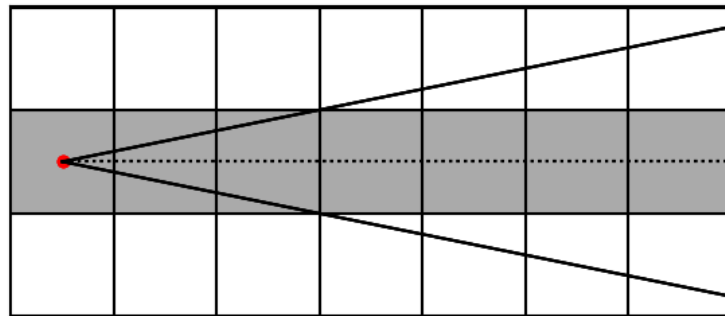
Figure 1: The figure illustrates one of the cones and its' axis, onto which the scerma in the voxel containing the tip of the cone is transported in the collapsed cone algorithm. In the first three columns (from left to right), the collapsed cone approximation is exact, meaning there is no further approximation than the discretization of the volume into Cartesian voxels. Beyond this, the collapsed cone approximation results in an overestimated dose contribution to voxels overlapping with the cone axis and an underestimated dose contribution to voxels overlapping with the cone but not its' axis.

The approximation limit the scerma in a voxel to be transported (i.e. attenuated and deposited) along the axes of j cones. The cones originating from a voxel i, of solid angles Ω_i, should fulfill the criteria $\sum \Omega_i$ of $\forall i$ equal 4π. Figure 1 illustrates one of these cones and its' axis, also called transport line. In the case where the Cartesian voxels occupy larger views than the solid angles of the cones, the collapsed cone approximation yields no further approximation [5, 15]. This is true for voxels close to the voxel containing the scerma to be spread. However, at greater distances, the opposite is true, i.e. the solid angle of the cone occupy larger views than the Cartesian voxels. The result is an overestimation of the dose in voxels overlapping with the cone axis and an underestimation in voxels overlapping with the cone but not its' axis, creating ray like structures originating from the voxel who's scerma was being spread. These artifacts, descended from the collapsed cone approximation, are called discretization artifacts[5].

The distance from the voxel containing the scerma to where the collapsed cone approximation is not exact depends on the size of the solid angles of the cones. A smaller solid angle of a cone yields a greater distance. With a greater distance the artifact is not only placed further from the scerma's origin but the severeness of the artifact is also decreased as the approximation becomes an approximation only for low dose values. However, with a decreased size of the solid angles, more cones has to be added to fulfill the criteria $\sum \Omega_i = 4\pi$, and hence, the number of transport lines increased. The more transport lines, the longer the calculation time.

In EBT discretization artifacts are seldom a problem as nearby voxels have scerma values of similar magnitude [15]. The overestimation in a voxel overlapping with a cone axis is counteracted by the underestimation in that voxel from another cone which axis does not cross the voxel. In brachytherapy, however, this is not the case. Steep fluence gradients, yielding large variations in scerma between near by voxels, results in over- and underestimations of different magnitude, and hence, they do not cancel each other out. The steeper the gradients, the more severe is the artifact.

It has been shown that the severeness of the discretization artifact is decreased as the number of active dwell positions are increased [7]. This is thought to be a result of decreased fluence gradients in multiple-source configurations and a "blurring effect" when artifacts from different dwell positions superimpose [7, 20]. The effect on the discretization artifact when increasing the number of dwell positions has been further investigated in this study.

2.2.2. The successive-scattering superposition method

As earlier discussed, the steep fluence gradients in brachytherapy enhance discretization artifacts when applying the collapsed cone superposition algorithm for scatter dose calculations [2, 15]. The successive-scattering superposition method, introduced by Carlsson and Ahnesjö [27], aim to reduce the influence of the steep gradients by dividing the scatter dose calculations into two steps, calculating the first-scattered dose (D_{1sc}) and the multiple-scattered dose (D_{msc}) separately [2, 15]. Here, D_{1sc} and D_{msc} are defined as the absorbed dose mediated by charged secondaries originating from once-scattered photons and multiple-scattered photons, respectively[6]. This separation yields a significant decrease

---

[5]The artifacts are also known as "the ray effect".

[6]Characteristic x-rays and Bremsstrahlung are considered as scattered photons of one-generation higher than the photons preceding the interacting electrons [2, 15, 27].

of the fluence gradients in the second calculation step, i.e. when calculating D_{msc}, and has shown to reduce the severeness of the discretization artifacts [15].

Figure 2 illustrates the steps in the successive-scattering superposition method, and below follows a description of each step.
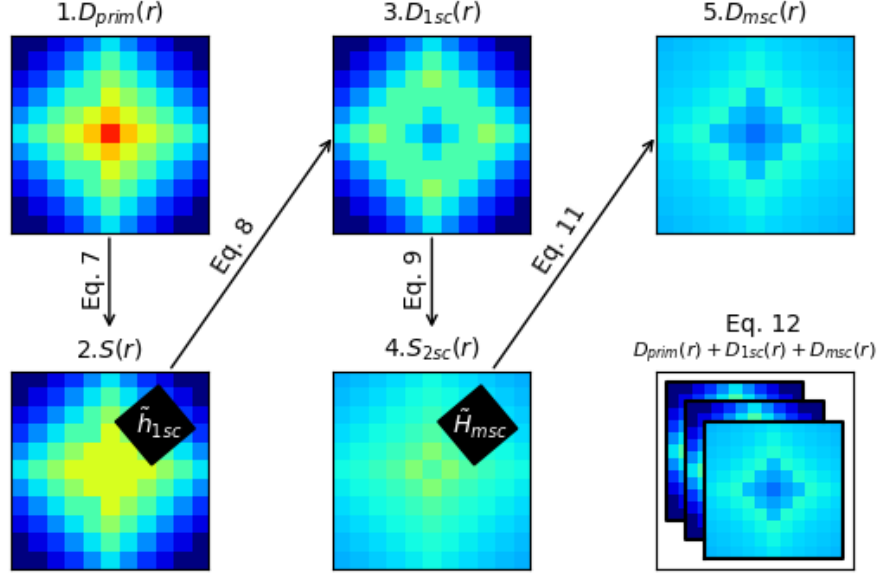

Figure 2: The figure illustrates the calculation steps in the successive-scattering kernel superposition method. D_{prim} is calculated through ray tracing. D_{1sc} and D_{msc} are calculated by superpositioning with with the first- ($\tilde{h}_{\mathrm{1sc}}$) and multiple-scattered ($\tilde{H}_{\mathrm{msc}}$) dose kernels, respectively. The equations 7-12 are presented in this section. The illustration is not to scale.

For the energy interval of photons in brachytherapy ($22\ \mathrm{keV} < \overline{E} < 662\ \mathrm{keV}$), the range of secondary electrons in water is short enough for charged particle equilibrium (CPE) to be a valid assumption [15]. The primary dose, D_{prim}, can therefore be approximated as the collision kerma, K_c, and hence, there is no need for superposition methods to be used for primary dose calculations [2, 15, 27]. By tracing rays from the source to each voxel, the primary dose per radiant energy emitted by the source, R, to a point $\mathbf{r} = (r, \theta, \phi)$ can be calculated as,

$$\frac{D_{\mathrm{prim}}(\mathbf{r})}{R} \overset{\mathrm{CPE}}{=} \frac{K_c(\mathbf{r})}{R} = a(\theta)\frac{1}{4\pi r^2}\frac{\overline{\mu}_{\mathrm{en}}(\mathbf{r})}{\rho(\mathbf{r})}e^{-\int_0^r \overline{\mu}(\mathbf{r}')r'\mathrm{d}r'}, \tag{6}$$

where $a(\theta)$ is a function describing source anisotropy, r is the distance from the source to the calculation point, $\rho(\mathbf{r})$ is the density at the calculation point and $\overline{\mu}_{\mathrm{en}}(\mathbf{r})$ and $\overline{\mu}(\mathbf{r})$ are the local average linear energy absorption and attenuation coefficients, respectively [2].

The primary dose distribution can then be used to calculate the scerma distribution, S, [2],

$$S(\mathbf{r}) \overset{\mathrm{CPE}}{=} \frac{\overline{\mu}(\mathbf{r}) - \overline{\mu}_{\mathrm{en}}(\mathbf{r})}{\overline{\mu}_{\mathrm{en}}(\mathbf{r})}D_{\mathrm{prim}}(\mathbf{r}). \tag{7}$$

The first-scattered dose, D_{1sc} is obtained by superposition of the scerma and a dose kernel,

$$\frac{D_{\mathrm{1sc}}(\mathbf{r})}{R} = \iiint\limits_V \frac{S(\mathbf{r}')}{R}\tilde{h}_{\mathrm{1sc}}(\mathbf{r}, \mathbf{r}')d^3r, \tag{8}$$

where $\tilde{h}_{1sc}(\mathbf{r})$ is the first-scatter dose kernel, normalized to the averaged energy released to first-scattered photons in a primary photon interaction [2, 15, 27]. The kernel describes the spatial dose distribution resulting from scerma released by primary photons interacting at the kernel's origin. As the spatial dose distribution depend on the primary photon direction, and brachytherapy beams are highly divergent, the kernel is spatially variant. Kernel tilting, i.e. maintaining the relative position between the kernel and the primary photon rays, is hence critical in the superposition calculation [27].

The first-scattered dose, $D_{1sc}(\mathbf{r})$, is in turn used to calculate the energy released from once-scattered photons to twice-scattered photons per unit mass S_{2sc},

$$S_{2sc}(\mathbf{r}) \overset{\text{CPE}}{=} \frac{\overline{\mu}_{1sc}(\mathbf{r}) - \overline{\mu}_{en,1sc}(\mathbf{r})}{\overline{\mu}_{en,1sc}(\mathbf{r})} D_{1sc}(\mathbf{r}), \tag{9}$$

where $\overline{\mu}_{en,1sc}(\mathbf{r})$ and $\overline{\mu}_{1sc}(\mathbf{r})$ are the averaged linear energy absorption and attenuation coefficient for once-scattered photons, respectively [2, 15, 27].

Unlike the first-scatter dose kernel $\tilde{h}_{1sc}$, the kernel for multiple-scattered dose calculations $\tilde{H}_{msc}$ has no unique direction for the orientation [2, 15]. This because the information about the direction of the first-scattered photons, interacting at the multiple-scattered kernels origin, is lost in the first-scatter dose calculation step in equation 9 [2, 15]. The isotropically averaged multiple-scattered kernel [15],

$$\tilde{H}_{msc,\ iso}(\mathbf{r}) = \frac{1}{2} \int_0^\pi \tilde{H}_{msc}(r, \theta) \sin\theta d\theta, \tag{10}$$

can hence be used to calculated the multiple-scattered dose as [2, 15, 27],

$$\frac{D_{msc}(\mathbf{r})}{R} = \iiint_V \frac{S_{2sc}(\mathbf{r}')}{R} \tilde{H}_{msc,\ iso}(\mathbf{r}, \mathbf{r}') d^3 r. \tag{11}$$

However, it has been shown that better results at 350 keV can be obtained if the angular information is keept and $\tilde{H}_{msc}$ is directed along the primary photon paths [2, 15].

The total dose is then calculated as [2],

$$D(\mathbf{r}) = D_{prim}(\mathbf{r}) + D_{1sc}(\mathbf{r}) + D_{msc}(\mathbf{r}). \tag{12}$$

2.2.3. Kernel parameterization

To carry out the superposition integrals of equation 8 and 10 with the collapse cone algorithm, the *energy deposition* kernels ($\tilde{h}_{1sc}(r, \theta)$ and $\tilde{H}_{msc}(r, \theta)$) has to be parameterized and rewritten as *energy fluence* kernels [2]. In this section analytical expressions together with kernel parameterization of $\tilde{h}_{1sc}(r, \theta)$ and $\tilde{H}_{msc}(r, \theta)$ are presented. In the implementation of the collapsed cone superposition algorithm the kernel parameters, to be introduced below, are fitted to Monte Carlo simulations in water phantoms. The analytical expression is hence only introduced to motivate the parameterization and to later, in the next section, explain how the parameters are scaled for non-water media. The parameterized first- and multiple-scattered energy fluence kernels, corresponding to the two energy deposition kernels, are also presented, but their derivation is out of the scope of this project and can be found else were [15]. Homogeneous media is assumed throughout this section.

The first-scatter dose kernel can be viewed as,

$$\tilde{h}_{1\text{sc}}(r,\theta) = \frac{1}{r^2}\frac{\mathrm{d}\sigma(\overline{E},\theta)}{\sigma(\overline{E})\mathrm{d}\Omega}\overline{\mu}_{\text{en,1sc},\theta} \times e^{-\overline{\mu}_{1\text{sc},\theta}r}, \tag{13}$$

where r is the distance from the primary photon interaction site (i.e. the kernel origin), $\overline{\mu}_{\text{en, 1sc},\theta}$ and $\overline{\mu}_{1\text{sc},\theta}$ are the averaged linear energy absorption and attenuation coefficients for once-scattered photons, respectively, $\mathrm{d}\sigma(\overline{E},\theta)/\mathrm{d}\Omega$ is the mean differential scattering cross section per unit solid angle for a photon spectrum of mean energy $\overline{E}$, and $\sigma(\overline{E})$ is the mean total cross section for primary photons of a mean energy $\overline{E}$ [2, 27]. The term $\mathrm{d}\sigma(E,\theta)/\sigma(E)\mathrm{d}\Omega$ can be interpreted as the fraction of scattered photons from a primary photon interaction, at $r = 0$, that are scattered at an angle θ with respect to the primary photon, into a solid angle $\mathrm{d}\Omega$. The decrease in the number of photons with increasing r, within a given solid angle, is solely caused by exponential attenuation [27].

From equation 13 it can be seen that the first-scatter dose kernel can be parametrizised with a monoexponential function,

$$\tilde{h}_{1\text{sc}}(r,\theta) = B_\theta e^{-b_\theta r}\Big/ r^2, \tag{14}$$

where B_θ and b_θ are the kernel parameters [2, 15, 27].

The corresponding energy fluence kernel to the first-scatter energy deposition kernel in equation 14 is given by [2, 15],

$$\tilde{h}_{\Psi,1\text{sc}}(r,\theta) = \frac{B_\theta}{b_\theta}e^{-b_\theta r}\Big/ r^2. \tag{15}$$

An approximate analytical expression for the multiple-scatter kernel $\tilde{H}_{\text{msc}}$ can be obtained by assuming the kernel to be rotational symmetric and divided into two parts,

$$\tilde{H}_{\text{msc}}(r) = \tilde{H}_{2\text{sc}}(r) + \tilde{H}_{\geq 3\text{sc}}(r), \tag{16}$$

where $\tilde{H}_{2\text{sc}}(r)$ and $\tilde{H}_{\geq 3\text{sc}}(r)$ are the kernels for dose deposited by charged secondaries following twice-scattered photons and three- or more times scattered photons, respectively [2]. As twice-scattered photons are released at the origin of $\tilde{H}_{\text{msc}}$, an analytical expression for $\tilde{H}_{2\text{sc}}(r)$ is straight forward,

$$\tilde{H}_{2\text{sc}}(r) = \frac{1}{4\pi r^2}\overline{\mu}_{\text{en,2sc}}e^{-\overline{\mu}_{2\text{sc}}r} = \frac{1}{r^2}k_1 e^{-\overline{\mu}_{2\text{sc}}r}, \tag{17}$$

where r is the distance from the kernel origin and $\overline{\mu}_{\text{en, 2sc}}$ and $\overline{\mu}_{2\text{sc}}$ are the linear energy absorption and attenuation coefficients for twice-scattered photons, respectively.

An analytical expression for $\tilde{H}_{\geq 3\text{sc}}(r)$ is somewhat harder to obtain as the third- and higher generation photons does not originate from the multiple-scatter kernel's origin. An approximate 1D expression can however be obtained by determining the energy released to photons of higher scatter generations from twice-scattered photons and distribute this energy in the radial direction with a 1D convolution with the with the forward directed kernel $e^{-\overline{\mu}_{\geq 3\text{sc}}r}$ [2].

Recalling that the kernel $\tilde{H}_{2\text{sc}}(r)$ describes the energy deposited by charged secondaries from twice-scattered photons, a kernel $\tilde{F}_{2\text{sc}}(r)$ describing the energy transferred to third-scattered photon can be obtained by chaining $\overline{\mu}_{\text{en, 2sc}}$ to $(\overline{\mu}_{2\text{sc}} - \overline{\mu}_{\text{en,2sc}})$ in equation 17, i.e.,

$$\tilde{F}_{2\text{sc}}(r) = \frac{1}{4\pi r^2}(\overline{\mu}_{2\text{sc}} - \overline{\mu}_{\text{en, 2sc}})e^{-\overline{\mu}_{2\text{sc}}r}. \tag{18}$$

The third- or higher order scatter kernel $\tilde{H}_{\geq 3\text{sc}}(r)$ can then be calculated as,

$$\tilde{H}_{\geq 3\text{sc}}(r) = \overline{\mu}_{\text{en},\geq 3\text{sc}} \int_0^r \tilde{F}_{2\text{sc}}(r')e^{-\overline{\mu}_{\geq 3\text{sc}}(r-r')}\mathrm{d}r' =$$

$$= \frac{1}{4\pi r^2}\frac{(\overline{\mu}_{2\text{sc}} - \overline{\mu}_{\text{en, 2sc}})\overline{\mu}_{\text{en},\geq 3\text{sc}}}{(\overline{\mu}_{\geq 3\text{sc}} - \overline{\mu}_{2\text{sc}})} \times (e^{-\overline{\mu}_{2\text{sc}}r} - e^{-\overline{\mu}_{\geq 3\text{sc}}r}) =$$

$$= \frac{1}{r^2}k_2(e^{-\overline{\mu}_{2\text{sc}}r} - e^{-\overline{\mu}_{\geq 3\text{sc}}r}), \tag{19}$$

where $\overline{\mu}_{\text{en},\geq 3\text{sc}}$ and $\overline{\mu}_{\geq 3\text{sc}}$ are the average linear energy absorption and attenuation coefficients for photons scattered three or more times [2].

An approximate 1D analytical expression for the multiple-scatter kernel is then obtained by substituting the expressions of $\tilde{H}_{2\text{sc}}(r)$ and $\tilde{H}_{\geq 3\text{sc}}(r)$ in equations 17 and 19 into equation 16,

$$\tilde{H}_{\text{msc}}(r) = \frac{1}{r^2}k_1 e^{-\overline{\mu}_{2\text{sc}}r} + \frac{1}{r^2}k_2(e^{-\overline{\mu}_{2\text{sc}}r} - e^{-\overline{\mu}_{\geq 3\text{sc}}r}) =$$

$$= \frac{1}{r^2}\left((k_1 + k_2)e^{-\overline{\mu}_{2\text{sc}}r} - k_2 e^{-\overline{\mu}_{\geq 3\text{sc}}r}\right). \tag{20}$$

From the analytical expression of $\tilde{H}_{\text{msc}}(r)$ in equation 20 it can be seen that the multiple-scatter kernel can be parametrizied using a biexponential function,

$$\tilde{H}_{\text{msc}}(r) = \frac{1}{r^2}\left(Ce^{-cr} + De^{-dr}\right) \tag{21}$$

where D, d, C and c are the kernel parameters that are fitted with Monte Carlo simulations [2]. The corresponding energy fluence kernel, normalized to the total radiant energy available for multiple-scatter dose, is given by [2],

$$\tilde{H}_{\Psi,\text{msc}}(r) = \left(\frac{C}{c}e^{-c\cdot r} + \frac{D}{d}e^{-d\cdot r}\right)\Big/ r^2. \tag{22}$$

2.2.4. Recursive stepping and heterogeneity scaling

In this section the recursive stepping method, to carry out the superposition integrals in equation 8 and 11 by the means of the collapsed cone superpositioning algorithm, will be explained. Prior to the calculation, each voxel should be assigned a scerma value. The transport of scerma from each voxel is then, as said, restricted to be transported on the axes of cones. All voxels have the same number of cones, where the axis of cone number n in each voxel is parallel to the axes of cone number n in the other voxels. The cone axes from different voxels are then arranged such that, for each set of cones n, with an axes in

direction θ_n, a set of parallel lines are obtained and each voxel is passed at least once by a line of direction θ_n. The combined length of lines in direction θ_n passing through a voxel i equals Δl_{max}, where Δl_{max} is the maximum step length that can be taken through voxel i in direction θ_n [6]. A lattice of lines in all directions θ_n are formed over the calculation grid. These lines are called transport lines. The use of transport lines increases the speed of the algorithm as it eliminates the need to follow each cone axis separately. The number of transport lines is proportional to the number of cone axis emerging from a voxel.

In the collapsed cone superposition algorithm each transport line m is followed separately, step by step [2]. The step length, Δl_i, is adjusted along the way so that each step exactly transverse 1 voxel, i.e,

$$\Delta l_i = r_i - r_{i-1}, \tag{23}$$

where r_{i-1} and r_i are the distances from the onset of the current followed transport line m to the point where transport line m enters and exit voxel i, respectively.

At each step i, of length Δl_i, energy release, energy transport and dose deposition is merged into the same calculation step [2]. A calculation step can be summarised with four sub-steps:

1. Determine the fraction (ε_i) of the radiant energy fluence the entrance of voxel i ($\hat{R}_{i-1}$) that remains at the exit of voxel i, and the fraction of $\hat{R}_{i-1}$ that is stopped in voxel i ($1 - \varepsilon_i$).

2. Calculate the radiant energy fluence released in voxel i onto transport line m ($\sigma_i \Delta l_i$), and determine the radiant energy fluence released in, and transported away from, voxel i ($\Delta \hat{R}_i$) and the radiant energy fluence released and stopped in voxel i ($\sigma_i \Delta l_i - \Delta \hat{R}_i$) along m.

3. Determine the total radiant energy fluence stopped in voxel i along m ($\hat{R}^*$) and calculate the dose contribution from transport line m to voxel i (D_m).

4. Determine the total radiant energy fluence leaving voxel i along m ($\hat{R}_i$) and repeat step 1 though 4 for voxel $i + 1$.

The steps are illustrated in Figure 3 and below follows a more detailed description of step 1 through 4 for the first-scattered dose calculation. The method of heterogeneity scaling will be introduced along the way.
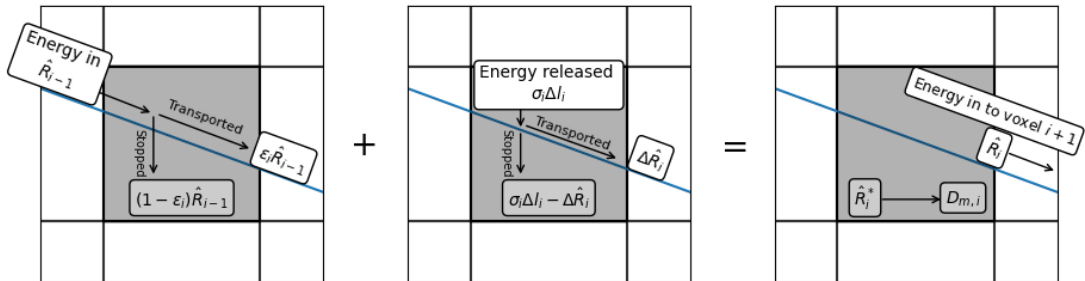

Figure 3: Illustration the sub-steps in a calculation step, taken along a transport line m in the collapsed cone superposition algorithm. The left figure illustrates sub-step 1, the middle figure illustrates sub step 2 and the right figure illustrates sub-step 3 and 4.

The first sub-step is simply performed by determination of the attenuation correction factor to transport $\hat{R}_{1sc,m,i-1}$ a distance Δl_i through voxel i. The factor is given by[7],

$$\varepsilon_i = e^{-\eta_{1sc,i}b_{\theta,i}\Delta l_i}, \tag{24}$$

where $b_{\theta,i}$ is the water derived kernel parameter in direction θ, where θ is the angle between the primary photon ray and transport line m, and $\eta_{1sc,i}$ is a heterogeneity scaling factor that scales the water derived parameter $b_{\theta,i}$ [6]. As can be seen from equation 13 and 14,

$$\eta_{1sc,i} = (\overline{\mu}_{1sc})_{\mathrm{med}_i} \Big/ (\overline{\mu}_{1sc})_{\mathrm{w}}, \tag{25}$$

where the index med_i and w denotes that the average linear attenuation coefficients, $(\overline{\mu}_{1sc})_{\mathrm{med}_i}$ and $(\overline{\mu}_{1sc})_{\mathrm{w}}$, are derived for the medium in voxel i and in water, respectively [2].

In sub-step 2, the amount of radiant energy locally released from voxel i into the cone of solid angle $\Delta\Omega_m$, per unit volume is determined as,

$$\sigma_i = S_{1sc,i}\rho_i\Delta\Omega_m \frac{B_{\theta,i}}{b_{\theta,i}}. \tag{26}$$

where $S_{1sc,i}$ and ρ_i are the scerma and density values of voxel i, and $B_{\theta,i}$ is the second water kernel parameter in direction θ [6]. The derivation of σ_i can be found elsewhere [5].

The radiant energy fluence released in, and transported away from voxel i is then given by [6],

$$\Delta\hat{R}_{1sc,i} = \int_{r_{i-1}}^{r_i} \sigma_i e^{-\eta_{1sc,i}b_{\theta,i}(r_i-s)}ds =$$

$$= \frac{\sigma_i}{\eta_{1sc,i}b_{\theta,i}}\left(1 - e^{-\eta_{1sc,i}b_{\theta,i}\Delta l_i}\right). \tag{27}$$

whereas the radiant energy fluence released in, and not transported away from voxel i is given by,

$$\int_{r_{i-1}}^{r-i} \sigma_i ds - \Delta\hat{R}_{1sc,i} = \sigma_i\Delta l_i - \Delta\hat{R}_{1sc,i}, \tag{28}$$

Here, $\sigma_i\Delta l_i$ is the total local radiant energy fluence released from voxel i along transport line m.

In sub-step 3, the amount of radiant energy fluence that stays in voxel i is determined as the sum of the radiant energy fluence entering the voxel and the radiant energy released in the voxel, that is not transported from the voxel, i.e

$$\hat{R}^*_{1sc,i} = (1 - \varepsilon_i)\hat{R}_{1sc,i-1} + (\sigma_i\Delta l_i - \Delta\hat{R}_{1sc,i}). \tag{29}$$

The dose contribution to voxel i from transport line m, is then given by,

$$D_{1sc,m,i} = \frac{1}{\Delta l_{\max}\rho_i} \frac{\chi_{1sc,i}}{\eta_{1sc,i}}\hat{R}^*_{1sc,i}, \tag{30}$$

---

[7]To be correct, the kernel parameter $b_{\theta,i}$ should be changed to a moving averaged to compensate for kernel tilting effects (see Ahnesjö et al. [6]).

where $\chi_{1\mathrm{sc},i}$ is a scaling factor for mass energy absorption [6]. From equation 13, the energy absorption scaling factor is defined as,

$$\chi_{1\mathrm{sc},i} = (\overline{\mu}_{\mathrm{en,1sc}})_{\mathrm{med}_i} \Big/ (\overline{\mu}_{\mathrm{en,1sc}})_{\mathrm{w}}, \tag{31}$$

where $(\overline{\mu}_{\mathrm{en,1sc}})_{\mathrm{med}_i}$ and $(\overline{\mu}_{\mathrm{en,1sc}})_{\mathrm{w}}$ are the averaged linear absorption coefficients in the medium of voxel i (med$_i$) and water (w), respectively [6]. In this definition of $\chi_{1\mathrm{sc},i}$, differences in angular shape of the kernel in water and in heterogeneous media has been neglected [2]. The ratio $\chi_{1\mathrm{sc},i}/\eta_{1\mathrm{sc},i}$ in equation 30, i.e,

$$\chi_{1\mathrm{sc},i}/\eta_{1\mathrm{sc},i} = \frac{(\overline{\mu}_{\mathrm{en,1sc}}/\overline{\mu}_{\mathrm{1sc}})_{\mathrm{med}_i}}{(\overline{\mu}_{\mathrm{en,1sc}}/\overline{\mu}_{\mathrm{1sc}})_{\mathrm{w}}} \tag{32}$$

scales the energy fraction deposited as dose in water to the energy fraction deposited as dose in medium.

In sub-step 4, the total radiant energy fluence at r_i, i.e. radiant energy present after traversing voxel i, is given by the sum [2, 6],

$$\hat{R}_{1\mathrm{sc},i} = \varepsilon_i \hat{R}_{1\mathrm{sc},i-1} + \Delta \hat{R}_{1\mathrm{sc},i}. \tag{33}$$

When all transport lines has been followed, the first-scattered dose to a voxel at location $\mathbf{r}$ is obtained by the sum of the dose contributions to the voxel from each transportline. That is,

$$D_{1\mathrm{sc}}(\mathbf{r}) = \sum_m D_{1\mathrm{sc},i(m),m}, \tag{34}$$

where the index $i(m)$ is used to mark that the step number i, taken to transverse the voxel at location $\mathbf{r}$, depend on which transport line m that is being followed.

As earlier explained (see equation 9), $D_{1\mathrm{sc}}(\mathbf{r})$ is in turn used to find $S_{2\mathrm{sc}}(\mathbf{r})$, and the same procedure as above is performed to find the multiple-scattered dose distribution $D_{msc}(\mathbf{r})$, using associated kernel parameters, scaling factors and scerma values.

However, as the multiple-scattered dose kernel is bioexponential (see equations 21 and 22), each calculation step i, i.e. sub-step 1 to 4, is carried out twice per step i along m, one time by substituting $B_{\theta,i}$ and $b_{\theta,i}$ with $C_{\theta,i}$ and $c_{\theta,i}$, respectively, and another time by replacing $B_{\theta,i}$ and $b_{\theta,i}$ with $D_{\theta,i}$ and $d_{\theta,i}$, respectively. The final multiple-scattered dose is then calculated as [6],

$$D_{\mathrm{msc}}(\mathbf{r}) = \sum_m (D_{\mathrm{msc,C},i(m),m} + D_{\mathrm{msc,D},i(m),m}). \tag{35}$$

Hence, two sets of scaling factors are defined for the multiple-scattered dose calculation, $\eta_{\mathrm{msc,i,C}}$ to correct the water derived kernel parameter c and $\eta_{\mathrm{msc,i,D}}$ to correct the water derived kernel parameter d. From eq 20, the scaling factors can be defined as,

$$\eta_{\mathrm{msc,i,C}} = (\overline{\mu}_{2\mathrm{sc}})_{\mathrm{med}_i} \Big/ (\overline{\mu}_{2\mathrm{sc}})_{\mathrm{w}}, \tag{36}$$

and

$$\eta_{\mathrm{msc,i,D}} = (\overline{\mu}_{\geq \, 3\mathrm{sc}})_{\mathrm{med}_i} \Big/ (\overline{\mu}_{\geq \, 3\mathrm{sc}})_{\mathrm{w}}. \tag{37}$$

However, in ACE a single scaling factor,

$$\eta_{\mathrm{msc,i}} = (\overline{\mu}_{\,\mathrm{msc}})_{\mathrm{med}_i} \Big/ (\overline{\mu}_{\,\mathrm{msc}})_{\mathrm{w}}, \tag{38}$$

is used in which the linear attenuation coefficients are averaged over the energies in the entire multiple-scattered spectrum.

Another difference in the calculation steps of the multiple-scattered dose is that the fraction of scaling factors in equation 30 ($\chi_{\mathrm{msc}}/\eta_{\mathrm{msc}}$) is set to unity to fulfill the requirement of energy balance/conservation of energy [2]. This is an approximation in which it is assumed that the ratios C/c and D/d are media independent. Note that since C and D are dependent on absorption coefficients, no scaling of these coefficients for non-water media is performed in the multiple-scattered dose calculation.

Equation 30 in calculation sub-step 3 is hence changed to

$$D_{\mathrm{msc, \, X},m,i} = \frac{1}{\Delta l_{\mathrm{max}} \rho_i} \hat{R}^*_{\mathrm{msc},i}, \tag{39}$$

where X equals C or D, when calculating the multiple scattered dose.

3. Materials & Methods

3.1. Dose Calculation Softwares

3.1.1. The Oncentra Brachy TPS by Elekta

As previously mentioned, a collapsed cone dose engine is available in the OcB TPS, implemented under the name Advanced Collapsed cone Engine (ACE). The commercially available OcB TPS version 4.6.0 by Elekta (Veenendaal, the Netherlands) has been used for ACE and TG-43 dose calculations. A research version of OcB 4.6.0 from the AAPM Task Group number 186 (TG-186), on model-based dose calculation algorithms in brachytherapy, has also been utilized [19]. The research version was made available for the project to allow for the three dose components (D_{prim}, D_{1sc} and D_{msc}, see section 2.2.2) to be studied separately.

The OcB TPS returns the dose to media in media ($D_{\mathrm{m,m}}$) and allows for ACE calculations to be performed with two different accuracy levels, standard and high. The differences in the algorithm between these two levels are the number of transport directions and the voxel grid utilized in the calculation step [4].

As the number of transport directions used in the calculation is proportional to the calculation time, as few transport directions as possible for the required accuracy is desired [20]. It has been shown by Carlsson Tedgren and Ahnesjö that for a fixed number of transport directions, the collapsed cone dose engine reaches a higher accuracy if a higher fraction of the total number of transport directions are utilized in the calculations of the first-scatter dose than in the multiple-scatter dose [20]. It was also shown by Carlsson Tedgren and Ahnesjö

that the severeness of the discretization artifact decrease in multiple-source configurations [20]. Therefore, the ACE algorithm always distributes the total number of transport directions unevenly between the first- and multiple-scattered dose calculations, and decreases the number of transport directions with an increasing number of dwell positions [4]. The number of transport directions used in the first-scatter (M_{1sc}) and the multiple-scattered (M_{msc}) dose calculations for the two accuracy levels are given in Table 1.

Table 1: The table gives the number of transport directions used in the fist-scattered (M_{1sc}) and multiple-scattered (M_{msc}) dose calculations, the margins (Δd_x) used to create the calculation grid, and the voxel size inside each calculation box, for the 2 accuracy levels of ACE [4]

| | Number of transport directions | | | |
| | Standard | | High | |
Number of DPs[a]	M_{1sc}	M_{msc}	M_{1sc}	M_{msc}
1	320	180	1620	240
2-50	320	180	720	240
51-150	240	128	500	200
151-300	200	80	320	180
≥ 300	180	72	240	128

| Square Voxel side cm | | Margin (cm) | | |
		Standard	High	High (Single DP[a])
0.1	Δd_1	1	8	10
0.2	Δd_2	8	20	20
0.5	Δd_3	20	35	50
1.0	Δd_4	50	50	100

[a]DP: Dwell Position

A calculation grid, independent of the planning CT, is used by ACE and is designed by the OcB TPS before dose calculation. To decrease calculation time, multiple-resolution voxelization is utilized, with smaller voxels in the vicinity of the dwell positions where a higher accuracy is required and an increased voxel size where dose levels are lower and a high accuracy is expected to be of less importance. The grid is calculated from the location of the dwell positions. First a rectangular bounding box, containing all active dwell positions is determined. From the bounding box, four new boxes ("ACE calculation boxes") are created by adding margins (Δd_i), equal in all six directions, to the bounding box. The voxel size is then increased from 1 mm in the smallest calculation box, to 10 mm in the largest calculation box. The four calculation boxes are illustrated in Figure 4 and the margins, together with the voxel size inside each box, are presented in Table 1 [4].

After TG-43 or ACE dose calculations, isodoses are immediately presented by the TPS. However, to save the calculated dose as an DICOM RD file, to compare with different treatment plans or to get dose statistics from the TPS, the dose in the calculation grid has to be transferred onto a new dose grid. The dimensions and voxel size of this new dose grid can be chosen by the user. The dose grids are single-resolution, i.e. the multi-resolution grid of ACE is transferred onto a single-resolution dose grid. The OcB TPS only transfer values of up to 800% of the prescribed dose (D_{per}) to the dose grid. This as such high doses are expected to be located inside a source, needle or catheter and are therefore clinically

irrelevant. Voxels that would yield a dose value of $> 8D_{\mathrm{per}}$ are assigned the value $8D_{\mathrm{per}}$ by the OcB TPS.
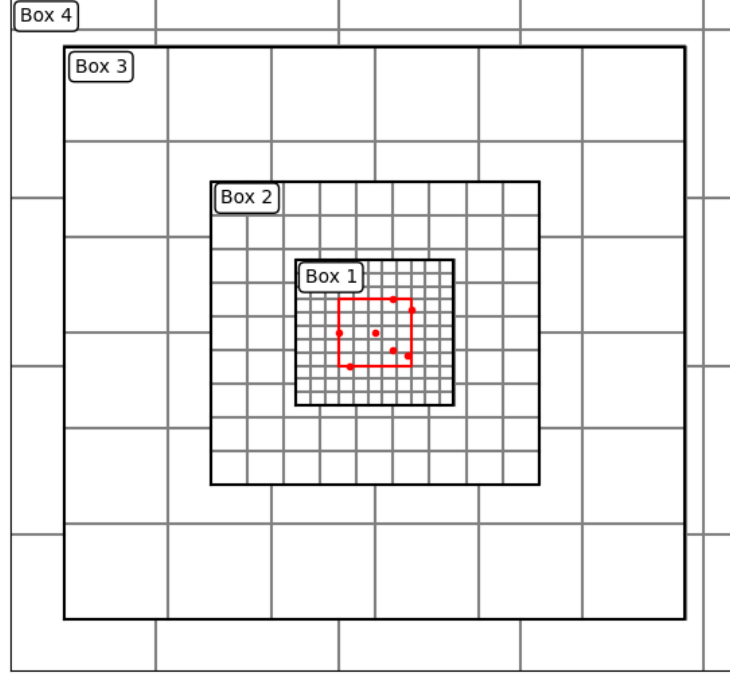

Figure 4: The figure illustrates the multiple-resolution calculation grid utilized by ACE. A bounding box (the inner red box) is determined from the location of active dwell positions (red dots). Four boxes, of different resolution, are designed by adding margins, equal in all six directions, to the bounding box. The margins and voxel sizes for each box are presented in Table 1. The figure is not to scale.

3.1.2. The ALGEBRA Monte Carlo platform

To evaluate ACE's ability to account for heterogeneities, a beta version of the GEANT4 based MC platform ALGEBRA (ALgorithm for heterogeneous dosimetry based on GEANT4 for BRAchytherapy) has been used. The accuracy of ALGEBRA has earlier been tested, both against the TG-43 formalism and against other MC codes with good results [28–30]. The specific version used in this study has been tested against the TG-43 formalism, see e.g. the master thesis of Maria Persson [31].

ALGEBRA utilizes a linear track length estimator (see Williamson [32]) to determine the particle fluence in a volume segment (i.e. a voxel in the scoring grid) from the total photon path length in that volume [28]. The absorbed dose is then estimated, under the assumption of CPE, as the collision kerma. The photon cut-off energy was set to 1 keV in this project. ALGEBRA allows for calculations of $D_{\mathrm{m,m}}$, or the absorbed dose to water in media ($D_{\mathrm{w,m}}$) [33]. The former has been used in this study to enable comparison between MC, ACE and TG-43 calculated doses.

To improve calculation speed ALGEBRA utilize multiple threading, where each thread make use of its' own source specific phase-space file. The phase-space files has to be generated prior to simulation and are created from particle tracking inside the source. As the files describes the particles position, direction and energy when exiting the source, the phase-space files are independent of the patient/phantom geometry and hence, only has to be generated once for each thread and source model. The need for particle tracking inside the source is in this way eliminated from the final simulation process [28].

The main type B (non-statistical) uncertainties in the dose estimates of ALGEBRA are the interaction cross section and the material and density assignments [33]. The first mentioned uncertainty, when precise materials are used, has been reported as approximately $\pm 2\%$ [33]. The second type B uncertainty is unknown. However, as the study uses virtual CT images in which material assignment, material composition and density is kept equal between dosimetry with MC and dosimetry with ACE, the uncertainty is expected to be of minor concern for dose comparison in this study. The statistical (type A) uncertainty is calculated by ALGEBRA using the "history-by-history" method [28]. The method has been described by Walters et al. [34].

ALGEBRA takes three files as input, a *dwell.dat* file, a *run.conf* file and a *phantom.egs* file. The *dwell.dat* file gives ALGEBRA the information of the location and dwell times of the dwell positions. The *run.conf* file specify the source model, the air-kerma strength and the number of photons to be simulated. The *phantom.egs* file gives the density and material of each voxel in the geometry grid. In this study the dimensions and resolutions of the scoring grid was equal to the geometry grid, defined in the *phantom.egs* file. The output of ALGEBRA is a *3ddose* file containing among other things, the dose distribution and the relative statistical uncertainty in each voxel.

3.2. The generic ^{192}Ir-MBDCA-WG source

A virtual generic HDR ^{192}Ir brachytherapy source has been developed by the AAPM Working Group on Dose Calculation Algorithms in Brachytherapy (WG-DCAB) for the purpose of MBDCA commissioning [30]. The source, together with test cases, afterloaders and vendor specific manuals for commissioning of MBDCA can be downloaded from the Source Registry [35]. The design of the generic MBDCA-WG source was constructed by F. Ballester et al. [30], taking into account 10 commercial ^{192}Ir HDR sources and selecting dimensions and materials for the generic source as representative to the majority of the commercial sources. The dimensions of the generic source are given in Table 2 and its' photon spectrum can be found in the article by Ballester et al. [30].

The MBDCA-WG source had been downloaded to the commercial OcB TPS at the time of MBDCA commissioning (2020, by Fanny Andersson [36]). The source calibration date[8] was April 1st, 2016 at 10:00:00 and the air kerma strength at the time of calibration was 36260.00 μGy m^2/ h. The same source had been downloaded on the research version of the OcB TPS. Here the calibration date was 23ed of January at 10:00:00 with an air kerma strength of 36260.00 μGy m^2/ h. The source had also been modeled in ALGEBRA and ALGEBRA has been tested against other MC codes with this source [30].

---

[8]Note that as the source is virtual no actual calibration has been performed. The calibration date and air kerma strength was chosen at commissioning (2020) in accordance to the vendor specific MBDCA commissioning user-guide.

Table 2: Properties of the generic ^{192}Ir-MBDCA-WG source [35].

Active length	0.35 cm	External diameter	0.1 cm
Total length	0.5 cm	Source to tip distance	0.06 cm
Active diameter	0.06 cm	Cable length	0.2 cm

3.3. Discretization artifact

3.3.1. Setup

To investigate the discretization artifact and its' dependence on the number of active dwell positions the commercial OcB TPS was used. TG-43 dose calculations were used as reference, hence, to fulfill TG-43 conditions, large water phantoms of volume 505x505x505 mm^3 were created in the TPS. The phantoms were created by constructing empty image series of size $x = y = z = 505$ mm with 101 slices, rows and columns, yielding a voxel size[9] of 5x5x5 mm^3. For each phantom a structure, covering the whole volume, was constructed and assigned the material of "water", using uniform density assignment. A three dimensional (3D) coordinate system was positioned in the phantoms with its' origin at the phantom center (slice 51, row 51, column 51).

Six different cases, with the MBDCA-WG source, were created. The number of dwell positions in each case was 1, 3, 5, 21, 27 and 125, respectively. All cases included a dwell position at the origin (x,y,z) = (0,0,0). In the cases of 3, 5 and 21 dwell positions, dwell positions were symmetrically added along a 2 cm long line. These cases will hereon be referred to as the line implants. In the cases of 27 and 125 dwell positions, dwell positions were symmetrically added in a cube of dimensions 2 cm x 2 cm x 2 cm and will be referred to as cube implants. The single dwell position will be called "point implant". The geometries are illustrated in Figure 5.
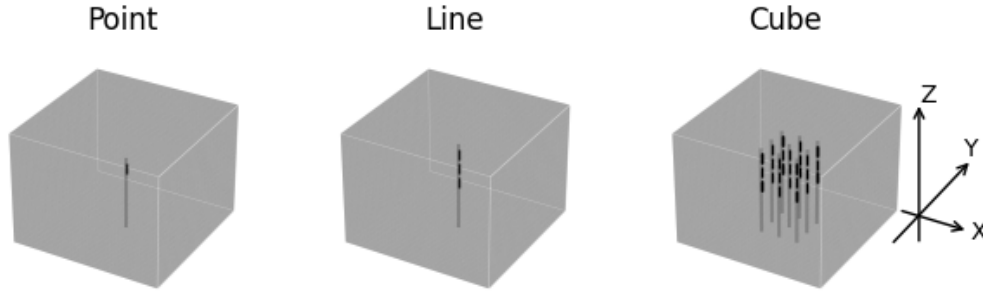

Figure 5: Schematic view of the three implants, i.e. point, line and cube. Gray lines represents the applicators and black cylinders illustrates the dwell positions. The figure is not to scale and the number of dwell positions in each implant was changed between different cases.

---

[9]The OcB TPS does not allow empty image series to be constructed with more than 500 slices, hence a voxel size of 1 mm^3 was not possible for a phantom of this size. This does however not affect the result when no heterogeneities are present as the resolution of the calculation grids in the OcB TPS are independent of the geometry grid (CT image).

In all of the six cases, the prescribed dose was set to 1 Gy at a point on the x-axis 1 cm from the closest dwell position. The normalization point for each case is given in Table 3. All dwell positions in a treatment plan were given equally long dwell times, i.e. equal weights were given to all dwell positions. This is unusual in clinical practice but was chosen to isolate the effect of an increased number of dwell positions on the discretization artifacts. The dwell times were automatically calculated by the OcB TPS to fulfill the dose prescription requirement when using the TG-43 formalism. The dwell times for each case are present in Table 3.

Table 3: Parameters used in the treatment plans for the six cases.

Source: 192-Ir-MBDCA-WG (generic)					
Treatment date: 01-02-2016, 10:00:00					
Air-kerma strength at the time of treatment: 36260.00 μGym^2/h					
Case Number	Implant Name	Number of DPs^a	Distance between DPs^a (mm)	Normalization point (mm)	Dwell time (s)
1	Point	1	-	(10,0,0)	8.94
2	Line	3	10	(10,0,0)	4.52
3		5	5	(10,0,0)	2.50
4		21	1	(10,0,0)	0.55
5	Cube	27	10	(20,0,0)	1.29
6		125	5	(20,0,0)	0.27

^{a}DPs: Dwell Positions

For each case the dose distribution was calculated using the TG-43 formalism and the ACE algorithm, with the standard accuracy level. The 12 dose calculations (2 for each case) were then transferred onto a grid of 301 slices, rows and columns, with a voxel size of 1 mm^3.

3.3.2. Analysis

For each of the six cases, the local dose difference ratio, $\Delta D_{\text{TG43}}^{\text{ACE}}$, was calculated with the TG-43 calculated dose used as the reference. The local dose difference ratio is defined as [29, 30, 37],

$$\Delta D_{\text{TG43}}^{\text{ACE}} = \frac{D^{\text{ACE}}(\mathbf{r}) - D^{\text{TG43}}(\mathbf{r})}{D^{\text{TG43}}(\mathbf{r})} \times 100 \ [\%], \tag{40}$$

where $D^{\text{ACE}}(\mathbf{r})$ and $D^{\text{TG43}}(\mathbf{r})$ are the dose at position $(\mathbf{r}) = (x, y, z)$ as calculated with ACE and TG-43, respectively. The local dose difference ratio serve as an indicator of the local dose discrepancies [29].

The local dose difference ratios has been displayed as color plots, 1D histograms and 2D histograms. In the color plots, the $z = 0$ plane was chosen to facilitate comparison between the cases, as the dose distribution in these planes have the most similar shapes between all six cases. In the 1D histograms, the distribution of local dose difference ratios in a volume of 10.1^3 cm^3, centered at the origin, was plotted with 10 bins per 1%. The local dose difference ratio in voxels overlapping fully or partially by an active dwell position has been omitted as they are clinically irrelevant. This by neglecting the values in voxels at

distances greater than 1 mm in the x- and y-plane and greater than 4 mm (5 mm) in the positive (negative) z-direction, from the center of each dwell position's active core.

From the histograms a number of statistical measures were extracted: the most probable value of $\Delta D_{\text{TG43}}^{\text{ACE}}$, the fraction of voxels yielding a $|\Delta D_{\text{TG43}}^{\text{ACE}}|$ value $\geq 2\%$, and the interval of $\Delta D_{\text{TG43}}^{\text{ACE}}$ in which 95% of the voxels were located. The two later measures were chosen to enable comparison with previous studies of ACE [7].

As no spatial information is contained in a 1D histogram, 2D histograms (as in Ma et al. [29]), were constructed. The purpose of the 2D histograms were to correlate the dose difference ratios with the distance to the center dwell position. Only the 1D plane $z = 0$ was considered in the 2D histograms. This to enable comparison between the cases as all cases had almost circular isodoses in the $z = 0$ plane. An exception is the isodoses for the cube implants at small radii.

For each case and each radii, the indexes fulfilling the criteria $x_i^2 + y_j^2 \leq (r - 0.5)^2$ and $x_i^2 + y_j^2 \geq (r + 0.5)^2$, were x_i is the position ($x \in [-150, 150]$) of row_i ($row \in [0, 300]$) and y_j is the position ($y \in [-150, 150]$) of $column_j$ ($column \in [0, 300]$), was found. The indexes were used to extract a circle from the dose difference ratio matrices, and for each extracted circle a histogram of $\Delta D_{\text{TG43}}^{\text{ACE}}$ (with 10 bins per 1%) was created and normalized to the number of voxels in the extracted circle. The histograms were then plotted with a color indicating the fractional number of voxels with a value $\Delta D_{\text{TG43}}^{\text{ACE}}$ at a distance r from the origin. The approximate location of the 20% and 5% isodose lines has also been drawn in the 2D histograms.

3.4. ACE's performance in cortical bone

3.4.1. Setup

To investigate ACE ability to account for cortical bone heterogeneities, three cases (A, B and C) were created. A virtual CT image of 301 rows, columns and slices, with a voxel size of 1 mm^3 where designed in python using the open source code *build_dicom.py* in "dicomutils" [38]. The CT image was imported to the research version of the OcB TPS were a structure, covering the entire CT image, was constructed and assigned the material "water". For each cases, a rectangular box of dimensions 3x3x2 cm^2 was created and assigned the material of "cortical bone". Uniform density assignment was utilized. The elemental composition and density of cortical bone is defined in the OcB TPS from the ICRU report 44 [39], as recommended by TG-186 [19]. The composition and density of cortical bone is presented in Table 5.

The bone heterogeneity was positioned with its' center at (0,0,-30 mm) in case A, at (0,0,-40 mm) in case B and at (0,0, -50 mm) in case C. The source configuration from case 5 in the discretization artifact study was used, (i.e, 27 dwell positions symmetrically placed in a cube centered at the origin) and the applicators were positioned parallel to the y-axis. This source configuration was chosen to keep the severeness of the discretization artifacts at a low level. The setup is illustrated in Figure 6 and the parameters utilized in the three treatment plans are given in Table 4.
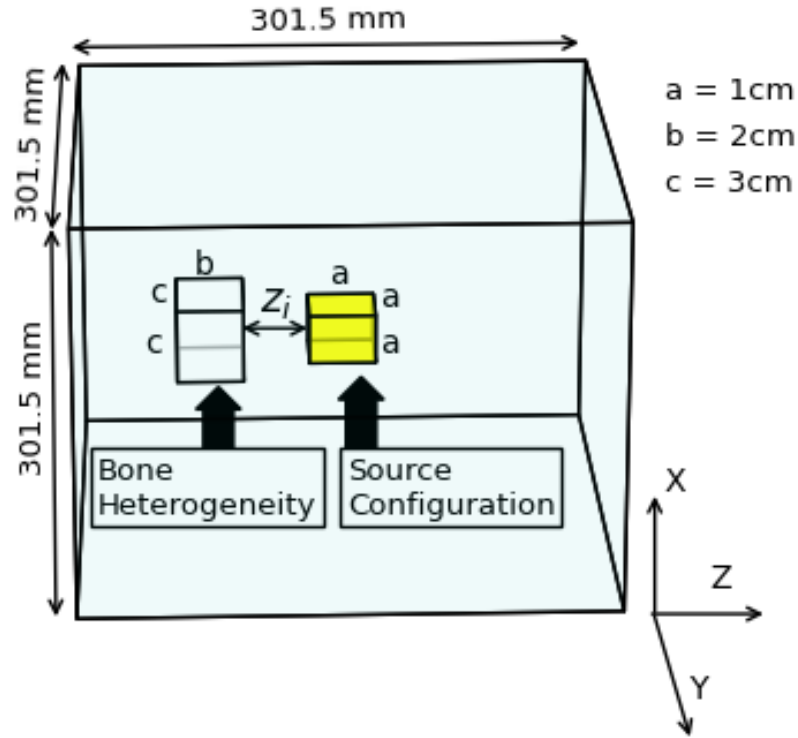
Figure 6: The setup used in the study of ACE ability to correct for a cortical bone heterogeneity. The distance Z_i between the source configuration and the cortical bone, was set to 10 mm, 20 mm and 30 mm in case A, B and C, respectively. The figure is not to scale.

Table 4: Treatment plan parameters used in case A, B and C.

Source: 192-Ir-MBDCA-WG (generic)			
Treatment date: 17-03-21, 10:00:00			
Air-kerma strength at the time of treatment: 29491.85 μGym^2/h			
Case	Distance between source configuration and bone (Z_i)	Normalization point (mm)	Dwell time (s)
A	10 mm	(0,0,20)	1.59
B	20 mm	(0,0,20)	1.59
C	30 mm	(0,0,20)	1.59

In all three cases the prescribed dose was set to 1 Gy at $(x, y, z) = (0,0,20$ mm$)$ and the dose distribution was calculated with both the TG-43 formalism and ACE with the high accuracy level. The dose distributions were transferred onto a dose grid of equal dimensions as the virtual CT images (i.e. 301 rows, columns and slices, with a voxel size of 1 mm). The cases where then extracted from the TPS.

The RP.dcm file from each case was used to create two of the input files to ALGEBRA (*dwells.dat* and *run.conf*) utilizing the python script given in appendix A. The virtual CT image serie, together with the DICOM structure files *RS.dcm* were imported to BrachyGUI, which was utilized to create the *phantom.egsphant* files. This was done by assigning each voxel in the CT image located inside the water box with the material and density of water, and then assigning each voxel in the CT image located inside the cortical bone structure with the material and density of cortical bone. The density and atomic composition of cortical bone was defined in ALGEBRA as in the OcB TPS (see Table 5).

For each case, the three files where used to calculate the dose distribution with ALGE-BRA (MC) using $3\text{x}10^8$ photons in the simulation.

Table 5: Elemental composition of cortical bone as defined in the OcB TPS and ALGEBRA [39].

Elemental composition (percentage by mass)									Mass density
H	C	N	O	Na	Mg	P	S	Ca	g cm^{-3}
3.4	15.5	4.2	43.5	0.1	0.2	10.3	0.3	22.5	1.92

3.4.2. Analysis

As the OcB TPS truncate dose values greater the 800 % of the prescribed dose, voxels given a value of 8 Gy (8 Gy or higher) has been removed from the OcB (MC) calculated dose distributions. Only a volume of 16x16x16 cm^3 centered at the origin, has been studied in the analysis. This to isolate the effect of the cortical bone heterogeneity from the general underestimation seen in ACE (see the results and discussion of part 1 of the study, sections 4.1 and 5), which increase in magnitude with an increasing distance from the dwell positions. In this volume, ACE's and MC's calculation grids were of equal resolution (1 mm^3 voxels).

A volume covering the bone heterogeneity (V_B=3x3x2 cm^3), a volume located behind (as viewed by the source) the bone heterogeneity (V_{BB}=3x3x1 cm^3) and a volume located in front of the bone heterogeneity (V_{IFB}=3x3x0.2 cm^3), were defined in python for each case. The dimensions and location, relative the bone heterogeneity, of the three volumes are illustrated in Figure 7. For each case, the mean dose to each one of the three volumes were calculated form the ACE calculated dose distribution ($D^{ACE}(\mathbf{r})$), the TG-43 calculated dose distribution ($D^{TG43}(\mathbf{r})$) and the MC calculated dose distribution ($D^{MC}(\mathbf{r})$).

The relative statistical uncertainty ($\sigma/D_{MC}(\mathbf{r})$) in $D_{MC}(\mathbf{r})$ was extracted from the *3ddose* files for the three cases and has been displayed as color plots in the y=0 plane. The mean relative statistical uncertainty in each of the three above defined volumes (see Figure 7) has been determined.

$D^{ACE}(\mathbf{r})$ and $D^{TG43}(\mathbf{r})$ was compared to $D^{MC}(\mathbf{r})$, utilizing the local dose difference ratio, with $D^{MC}(\mathbf{r})$ as the reference, i.e.,

$$\Delta D_{\text{MC}}^{\text{k}}(\mathbf{r}) = \frac{D^k(\mathbf{r}) - D^{MC}(\mathbf{r})}{D^{MC}(\mathbf{r})} \times 100 \ [\%], \tag{41}$$

where k equal ACE or TG-43. The results has been displayed as color plots in the y=0 plane. In the 2 volumes V_B and V_{BB}, histograms of $\Delta D_{\text{MC}}^{\text{ACE}}(\mathbf{r})$, with 10 bins per % has also been determined.
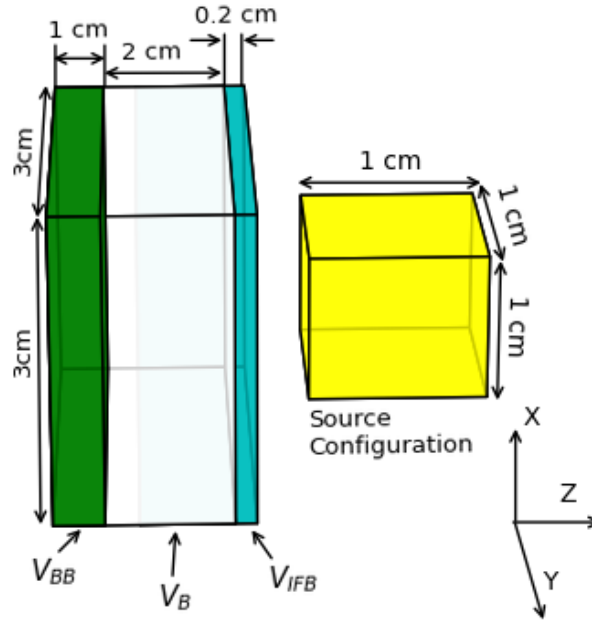
Figure 7:   Illustration of the three volumes, V_B=3x3x2 cm³, containing the bone heterogeneity, V_{BB}=3x3x1 cm³, located behind the bone heterogeneity and V_{IFB}=3x3x0.2 cm³ located in front of the bone heterogeneity. The figure is not to scale.

For each case, two volumes of equal dimensions and with the same x and y positions as V_B and V_{BB}, respectively, were positioned at equal distance, but at the opposite side of the z=0 plane. These volumes were taken as representatives of the dose distribution in V_B and V_{BB} in an all water case. This as the bone heterogeneity was expected to have a neglectable effect on the dose distribution at positive z values, and the dose distribution for positive z values was assumed to be a mirrored distribution of that for negative z values, if no heterogeneity had been present. Histograms of $\Delta D_{\mathrm{MC}}^{\mathrm{ACE}}(\mathbf{r})$ inside these volumes were constructed for comparison.

For each case and dose calculation method (ACE, TG-43, and MC), dose profiles were extracted along the 1D line $x = y = 0$ and $z =$[-75 mm,75 mm], from the dose distribution. The profiles were obtained by calculating the mean value of voxels in a square of 5x5 mm², centered at $x = y = 0$ and z_i, for each step i of length 1 mm along the z-axis. The mean value of 25 voxels was chosen to reduce statistical fluctuations in the dose profiles from $D_{MC}(\mathbf{r})$.

The profiles from $D^{MC}(\mathbf{r})$ ($D^{MC}(z)$) and $D^{ACE}(\mathbf{r})$ ($D^{ACE}(z)$) has been plotted as a function of the absolute distance from the origin $|z|$, and normalized to the profile from $D^{TG43}(\mathbf{r})$ ($D^{TG43}(z)$). The normalization was performed to get rid of steep dose gradients and enhance the effects of the bone heterogeneity on the dose distribution. The profiles for positive z values were assumed to represent the profile for negative z values, if no cortical bone heterogeneity had been present.

The three components in $D^{ACE}(\mathbf{r})$ ($D_{\mathrm{prim}}(\mathbf{r})$, $D_{\mathrm{1sc}}(\mathbf{r})$ and $D_{\mathrm{msc}}(\mathbf{r})$) has been extracted from the OcB TPS. For each case, and each component, the dose profile along the same 1D line as above has been obtained and plotted in the same manner.

4. Results

4.1. Discretization artifacts

Figure 8 shows color plots of ΔD_{TG43}^{ACE} for the six cases (see Table 3) in the $z = 0$ plane (color plots of the other planes can be found in appendix B). The discretization artifacts manifest itself in the color plots as ray-like structures, containing positive ΔD_{TG43}^{ACE} values. One (or two in the case of the cube implants) square is clearly visible in each one of the color plots resulting from the multiple-resolution voxelization grid utilized by ACE (see section 3.1.1).
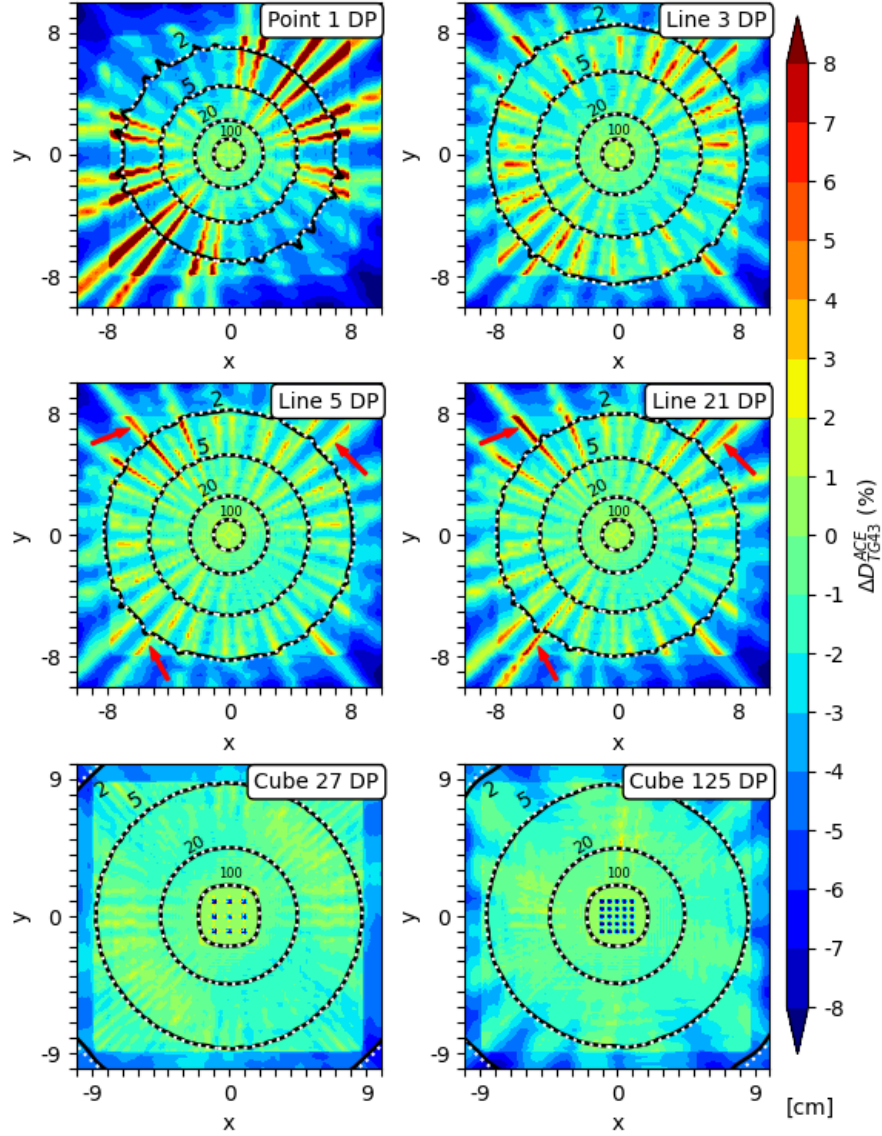

Figure 8: Color plots of ΔD_{TG43}^{ACE} in the $z = 0$ plane for the six cases presented in Table 3. The 100%, 20%, 5% and 2% isodose lines from the TG-43 calculated dose distribution (white dots) and ACE calculated dose distribution (black lines) are also presented.

From the color plots and the histograms in Figure 9 it can bee seen that, for all cases, the majority of ΔD_{TG43}^{ACE} values are less than zero, indicating that ACE systematically underestimates the dose as compared to TG-43. This is also evident by the statistical analysis presented in Table 6, where the most probable values of ΔD_{TG43}^{ACE} are $\leq 0\%$ (from -0.6 % for case 3 and 4 to -1.8% for case 1) and the range of ΔD_{TG43}^{ACE} in which 95% of the voxels can be found is asymmetrically placed around 0%, stretching farther down on the negative scale (e.g. $[-3\%, 1.4\%]$ for case 3).
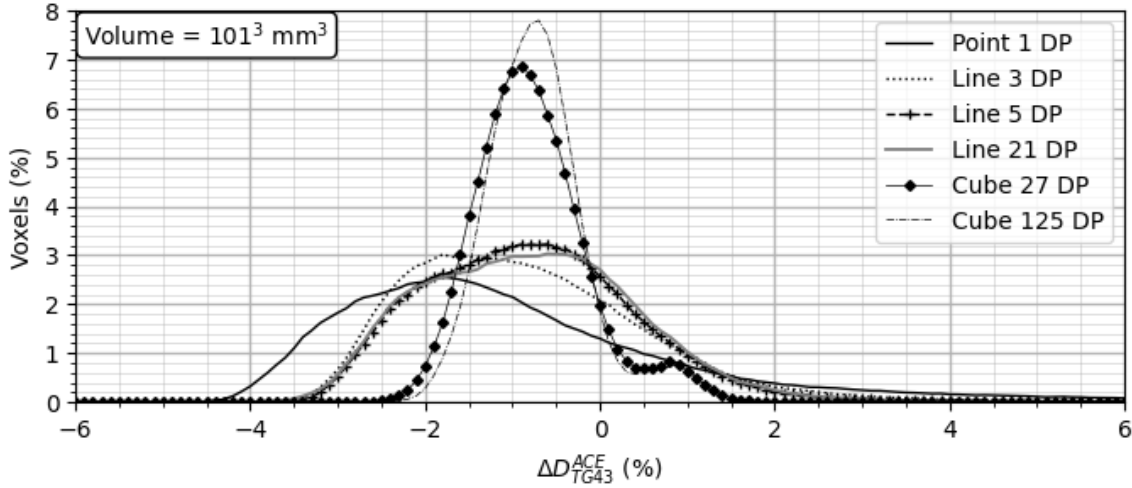

Figure 9: Histograms of ΔD_{TG43}^{ACE} with 10 bins per 1%, for the six cases presented in Table 3. The histograms are calculated from a volume of 101^3 mm^3 centered at the phantoms origin.

Comparing the cases to one another, it is clear that the agreement between ACE and TG-43 is improved as the number of dwell positions are increased from 1 to 3 to 5 and from 5 to 27. This is shown by the color plots, where the ray like structures contain less and less ΔD_{TG43}^{ACE} values over 1% as the number of dwell positions are increased. The color plots also show how the artifacts turns narrower and increase in number as the implant geometry is changed from the point implant to the line implant and to the cube implant.

Table 6: Statistical measures of ΔD_{TG43}^{ACE} for the six cases, in a volume of 101 mm^3 centered at the origin of the phantom. DPs stand for dwell positions.

Case number	Implant Name	Number of DPs	Most prob. value (%)	Fraction of voxels that differ more than 2% (%)	Interval in witch 95% of the voxels are located (%)
1	Point	1	-1.8	42.6	[-4.1 , 4.0]
2	Line	3	-1.8	23.1	[-3.1 , 1.8]
3		5	-0.6	17.8	[-3.0 , 1.4]
4		21	-0.6	18.6	[-3.0 , 1.4]
5	Cube	27	-0.9	1.2	[-2.0 , 0.9]
6		125	-0.7	0.6	[-1.8 , 1.0]

From the histogram and the statistical analysis, the improved agreement between ACE and TG-43 is reflected by the narrower range of ΔD_{TG43}^{ACE} in which 95% of the voxels are found (from $[-4.1\%, 4\%]$ for 1 DP to $[-2.0\%, 0.9\%]$ for 27 DP). The number of voxels that

differ more than $\pm 2\%$ also decrease from case 1 (42.6%) to case 2 (23.1%) to case 3 (17.8%) and from case 3 to case 5 (1.2%).

If judged from the histogram and the statistics in Table 6 the agreement is also improved when incensing the number of dwell positions from 27 to 125. However, the color plots reveals more pronounced artifacts in case 6 than in case 5 (as seen in between the 5% isodose line and the edge of the second calculation box). This is most probably caused by the fewer transport directions used in ACE when the number of dwell positions exceeds 50. Hence, a study of the artifacts behavior when increasing the number of dwell positions from ≤ 50 to > 50, using the clinical TPS, restricts the comparison to be limited to the general performance of the OcB TPS rather than the behavior of ACE itself.
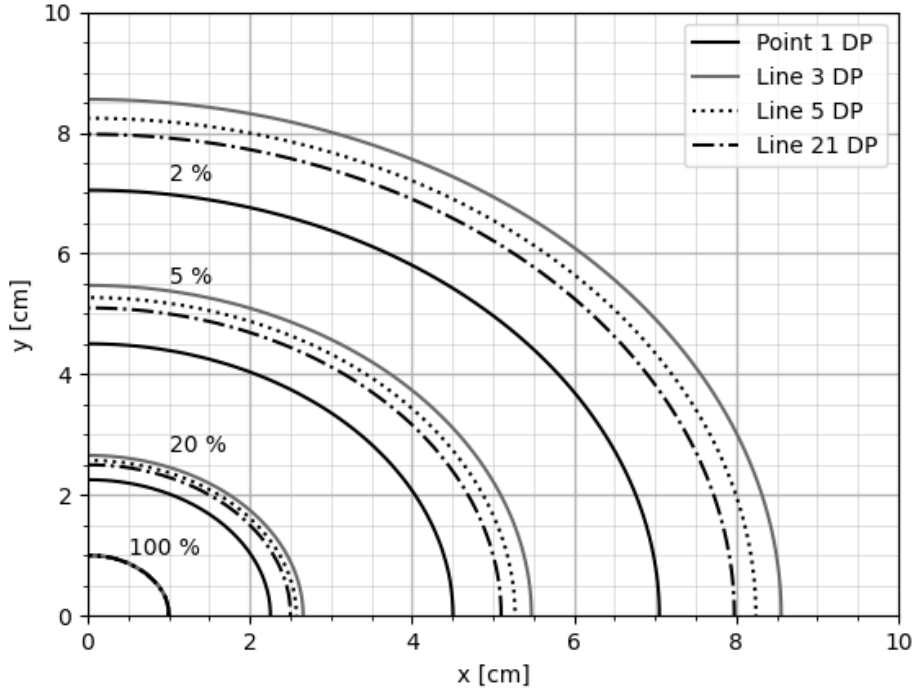

Figure 10: The TG-43 calculated isodoses for case 1 to case 4 (see Table 3). The plot show how the dose gradients decrease when going from a single dwell position to three dwell positions on a line and then increase as more dwell positions are added in the line implant.

Comparing case 3 to case 4, increasing the number of dwell positions from 5 to 21 in a line implant did not result in an improved agreement between ACE and TG-43 dose calculations. If only considering the color plots, some of the ray like artifacts (e.g. the artifacts pointed out by arrows in Figure 8) appears worse (contain higher ΔD_{TG43}^{ACE} values) in the case including 21 dwell positions. From Table 6 it can be seen that the number of ΔD_{TG43}^{ACE} values yielding an absolute value of $\geq 2\%$ increased with 0.8% when increasing the number of dwell positions, whereas the interval in which 95% of the ΔD_{TG43}^{ACE} values were located remained constant.

Figure 10 illustrates how the dose gradients (as calculated with the TG-43 formalism) in the $z = 0$ plane decrease when increasing the number of dwell positions from 1 to 3, and how the dose gradients then increase as more dwell positions are added to the line implant.
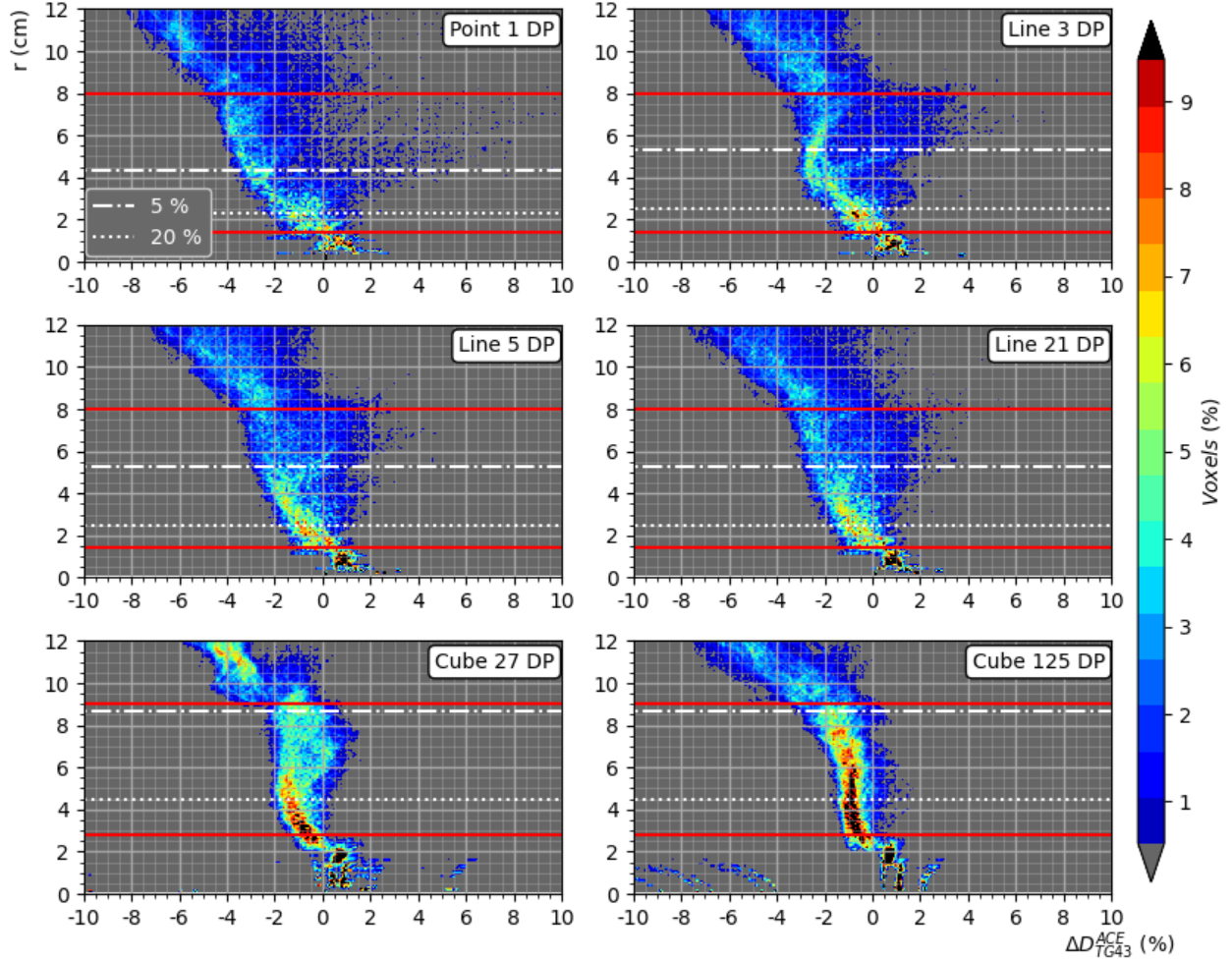
Figure 11: 2D histograms of the distance to the origin r versus $\Delta D_{\mathrm{TG43}}^{\mathrm{ACE}}$. The red lines indicates the interval in which where only voxels belonging to ACE's second calculation box were extracted. The isodose lines are taken as perfectly symmetric around the origin and are drawn at their approximate location.

Figure 11 shows the 2D histograms of $\Delta D_{\mathrm{TG43}}^{\mathrm{ACE}}$ in the z=0 plane for the six cases. Solid red lines have been drawn in the figures to indicate the interval in which where only voxels of size 2 mm were used in the ACE calculations (i.e. the circles intersecting with extracted voxels are completely contained in the second calculation box). From the 2D histograms it can be seen that the majority of ΔD_{TG43}^{ACE} in the vicinity of the source are positive, i.e. ACE overestimates the dose as compared to TG-43. The opposite is true for voxels outside the inner calculation box.

Focusing only on the second calculation box (in between the red lines in the 2D histograms), in case 1 voxels containing ΔD_{TG43}^{ACE} values over 2% were mainly found outside the 5% isodose line. This can also be seen in the color plots as the ray artifacts get stronger at this distance. Increasing the number of dwell positions from 1 to 3 significantly reduced the high (over 4%) ΔD_{TG43}^{ACE} values and created a more distinct bulk of positive ΔD_{TG43}^{ACE} values on the 2D histogram between the 5% isodose line and the edge of the second box. Increasing the number of dwell positions from 3 to 5 decreased the size of this bulk to

mainly contain values under 2%. This can also be seen in the color plots as less voxels with a value over 2% are seen in the case with 5 dwell positions than in the case with 3 dwell positions. It can also be seen that the underestimation of ACE as compared to TG-43 in the interval between the 20% and 5% isodoses decreased when increasing the number of dwell positions from 3 to 5.

No significant difference was seen in the 2D histograms when increasing the number of dwell positions in a line implant from 5 to 21.

In the cases with cube implants (27 and 125 dwell positions) the bulk, indicating the high over estimations in the ray artifacts, disappeared and the overall distribution of ΔD_{TG43}^{ACE}, at all radii considered, became narrower. Some very high (above 4%) and some very low (below -4%) values can be seen at small radii ($r \leq 2$ cm). These are values of ΔD_{TG43}^{ACE} located in or very close to a source and should not be considered when comparing these cases to the others. Values of ΔD_{TG43}^{ACE} in a source are not as pronounced in the other cases as the chose of the $z = 0$ plane only include 1 dwell position placed at the origin for the cases with point and line geometries. As earlier pointed out, the values in or very close to a dwell position are clinically irrelevant (see section 3.1.1).

4.2. ACE's performance in cortical bone

In the following section the results from the "cortical bone heterogeneity study" will be presented. Any prepositions made in this section should be interpreted as viewed from the origin of the phantom.
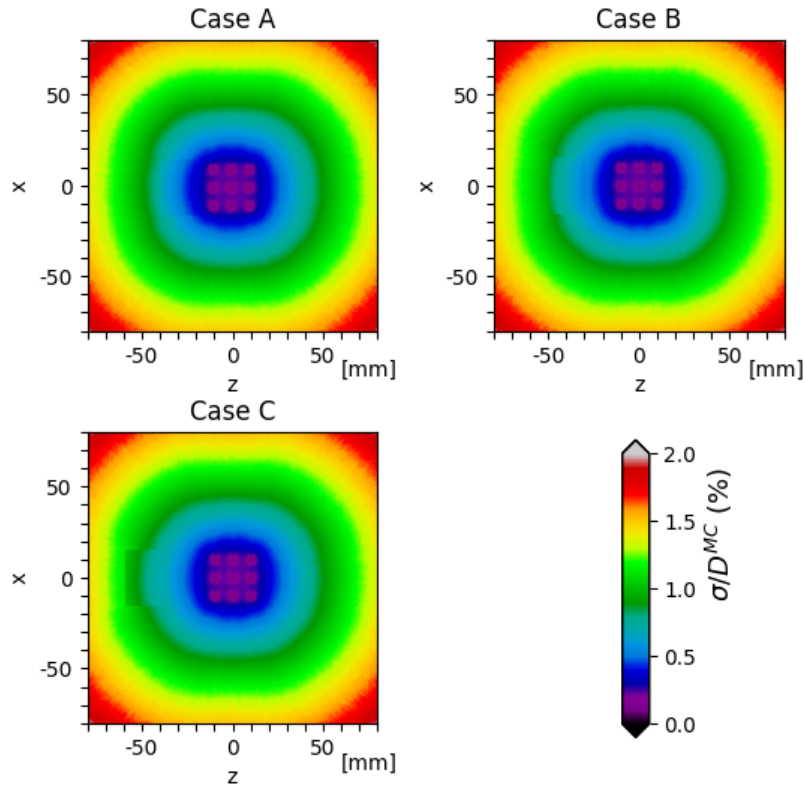

Figure 12: Color plots in the y=0 plane of the relative statistical uncertainty in the MC calculated dose distributions in case A, B and C.

Figure 12 displays the relative statistical uncertainty, σ_i/D^{MC}, in the $y = 0$ plane for the MC calculated dose distributions of case A, B and C. As can be seen, the statistical uncertainty in the volume of interest (a square of 16x16x16 cm³ centered at the origin) was kept below 2%. A rectangular shape is visible in all three cases at the location of the bone heterogeneities. It can be seen that the statistical uncertainty in the y=0 plane in the heterogeneities (inside the rectangular structure) were kept well below 1.5%. The mean statistical uncertainty in the volumes V_B, V_{BB} and V_{IFB} (defined in section 3.4, Figure 7) are presented in Table 7.

Figure 13 shows color plots of the local dose difference ratio ΔD_{MC}^{TG43} in the $y = 0$ plane for case A, B and C. At positions where the bone heterogeneity has no significant effect on the dose distribution, $D^{TG43}(\mathbf{r})$ and $D^{MC}(\mathbf{r})$ were expected to be in agreement, i.e. $\Delta D_{MC}^{TG43} \approx 0\%$. This was true for e.g. voxels located in front of the bone heterogeneity, with the exception of voxels located in or close to a dwell position.
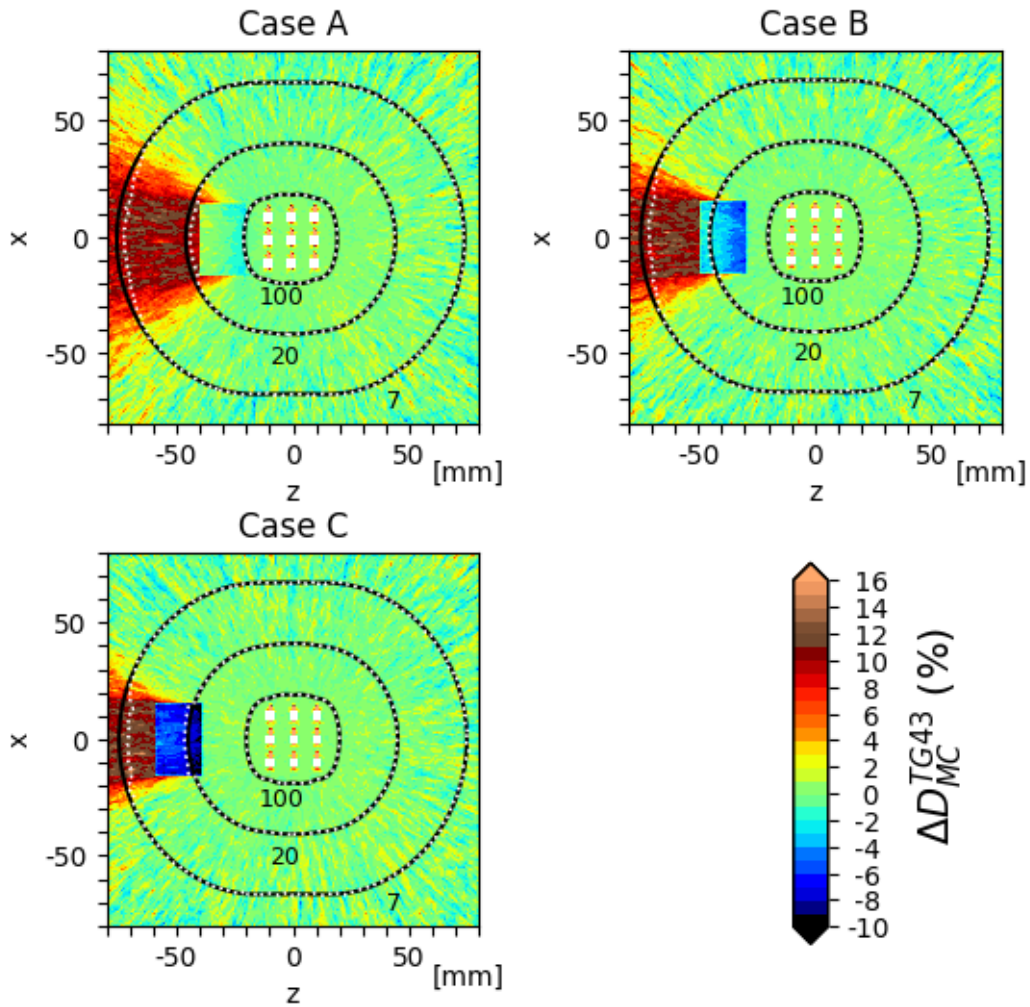

Figure 13: Color plots of D_{MC}^{TG43} in the $y = 0$ plane for case A, B and C. Voxels with a dose value of 8 Gy or higher has been omitted, and assigned the color white. Isodose lines for the 100%, 20% and 7% level, as calculated with TG-43 (black solid lines) and MC (white dotted lines) are presented in the plots.

In the cortical bone heterogeneity TG-43 underestimated the dose. The magnitude of the underestimation was greatest in the proximal part of the bone. As the heterogeneity was positioned farther away from the source configuration, the magnitude of the underestimation increased. At positions in the shadow of the bone, i.e. at points to which photons has to travel through the heterogeneity to reach, TG-43 overestimated the dose by approximately 3-14%.

The 100%, 20% and 7% isodose lines from $D_{MC}(\mathbf{r})$ (white dotted lines) and $D_{TG43}(\mathbf{r})$ (black solid lines) are also drawn in the color plots in Figure 13. As can be seen, the overestimations made by TG-43 resulted in an error on the 20% and 7% isodose lines in case A, and on the 7% isodose line in case B and C. The underestimations in the bone heterogeneity had no visible effect on the 20% isodose line in case B and a small but discernible effect on the 20% isodose line in case C.

The left column of Figure 14 shows color plots in the y=0 plane of ΔD_{MC}^{ACE}. It is clear from the figure that ACE underestimated the dose to cortical bone in all three cases. As can be seen in the color plots, the underestimations in the heterogeneity were of greater magnitude than the general underestimation in ACE (see section 4.1 and 5). This is also shown by the histograms in Figure 15 (left column), where the distribution of ΔD_{MC}^{ACE} values in V_B (black solid lines) contained a higher fraction of negative ΔD_{MC}^{ACE} values, of greater magnitude, than the distribution of ΔD_{MC}^{ACE} values in V_B in an all water case[10] (gray dashed lines).

The magnitude of the underestimation seen in $D^{ACE}(\mathbf{r})$ in the cortical bone increased as the bone was positioned further away from the origin. For example, as can be seen in the histograms, ΔD_{MC}^{ACE} took values down to approximately -10% in case A and -16% in case C. The underestimation can also be seen on the 20% isodose line, drawn in Figure 14, in case B and C. The 20% isodose line from $D^{MC}(\mathbf{r})$ (white dotted line) reached slightly farther into the bone than the 20% isodose line from $D^{ACE}(\mathbf{r})$ (black solid line).

Behind the heterogeneity ACE and MC showed comparable results. For all three cases, the 7% isodose line from the MC (white dotted lines) and ACE (black solid lines) calculated dose distributions, drawn in the color plots in Figure 14, were in agreement at all locations in the y=0 plane. However, in this region, the number of voxels in which ACE overestimated the dose increased. As can be seen in the histograms in Figure 15 (right column), the distribution of ΔD_{MC}^{ACE} values in the volume V_{BB}, in the heterogeneous geometry (black solid lines), as compared to the distribution of ΔD_{MC}^{ACE} in the volume V_{BB}, in an all water case (gray dashed lines), was shifted in the positive direction.

The right column of Figure 14 shows the extracted dose profiles $D^{MC}(z)$ (dotted lines) and $D^{ACE}(z)$ (solid lines), normalized to $D^{TG43}(z)$, along the horizontal line $z\epsilon$[-75mm, 75mm], indicated in corresponding color plot. As motivated in section 3.4.2, the profiles for positive z values are assumed to represent the profile for negative z values in an all water case.

---

[10]Note that the V_B (and V_{BB}) without the heterogeneity is not actually taken from an all water case but is an representative volume (see section 3.4.2)
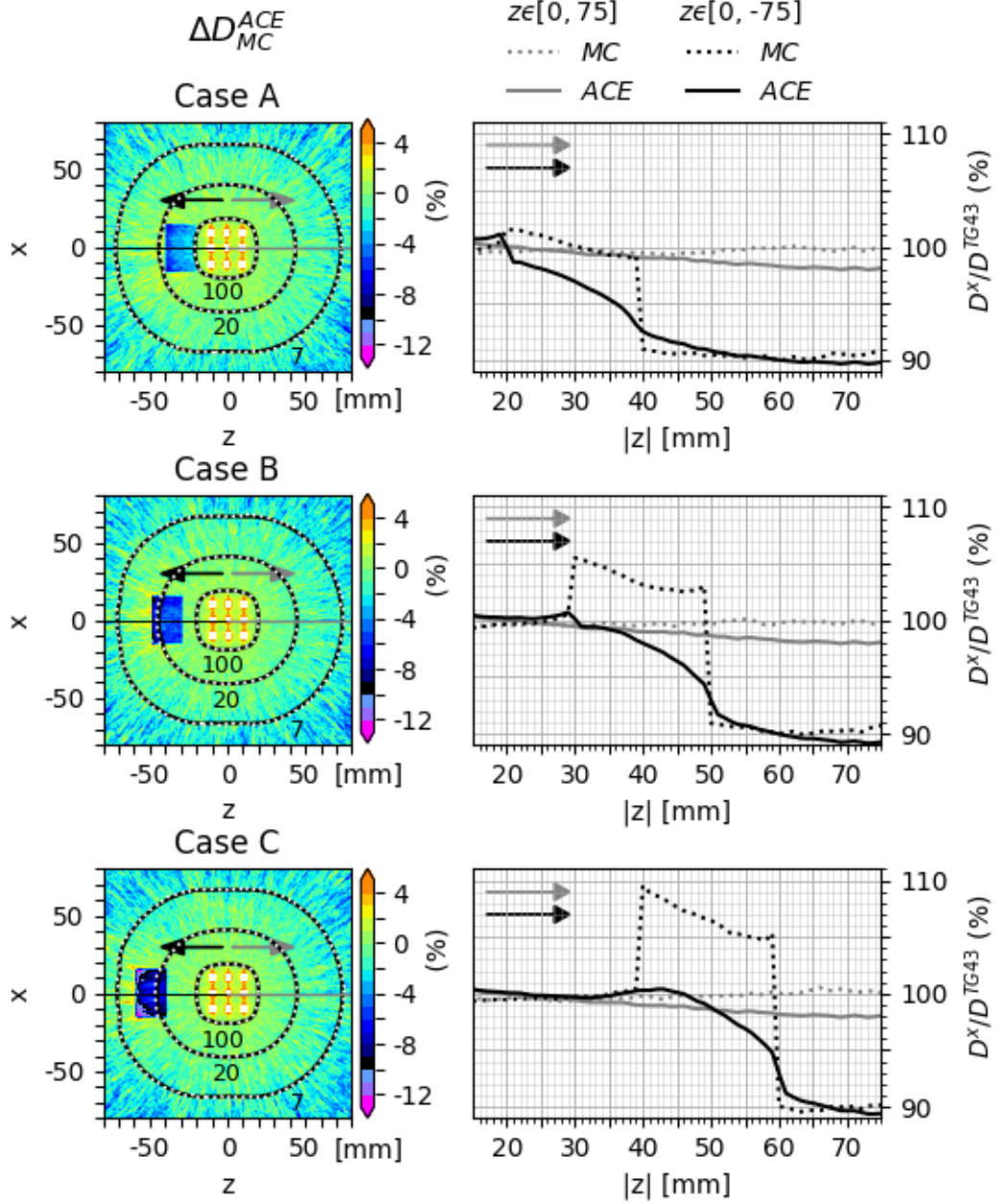
Figure 14: Left Column: Color plots of D_{MC}^{ACE} in the $y = 0$ plane for case A, B and C. Isodose lines for the 100%, 20% and 7% levels, as calculated with ACE (black solid lines) and MC (white dotted lines) are presented in the plots. Right column: Dose profiles of the MC calculated dose distribution (dotted lines) and the ACE calculated dose distribution (solid lines) along the horizontal line $z\epsilon[-80mm, 80mm]$, plotted as a function of absolute distance from the origin. Gray lines are the profiles for positive values of z, whereas black lines are the profiles for negative values of z. The profiles have been normalized to the dose profile from the TG-43 calculated dose distribution.

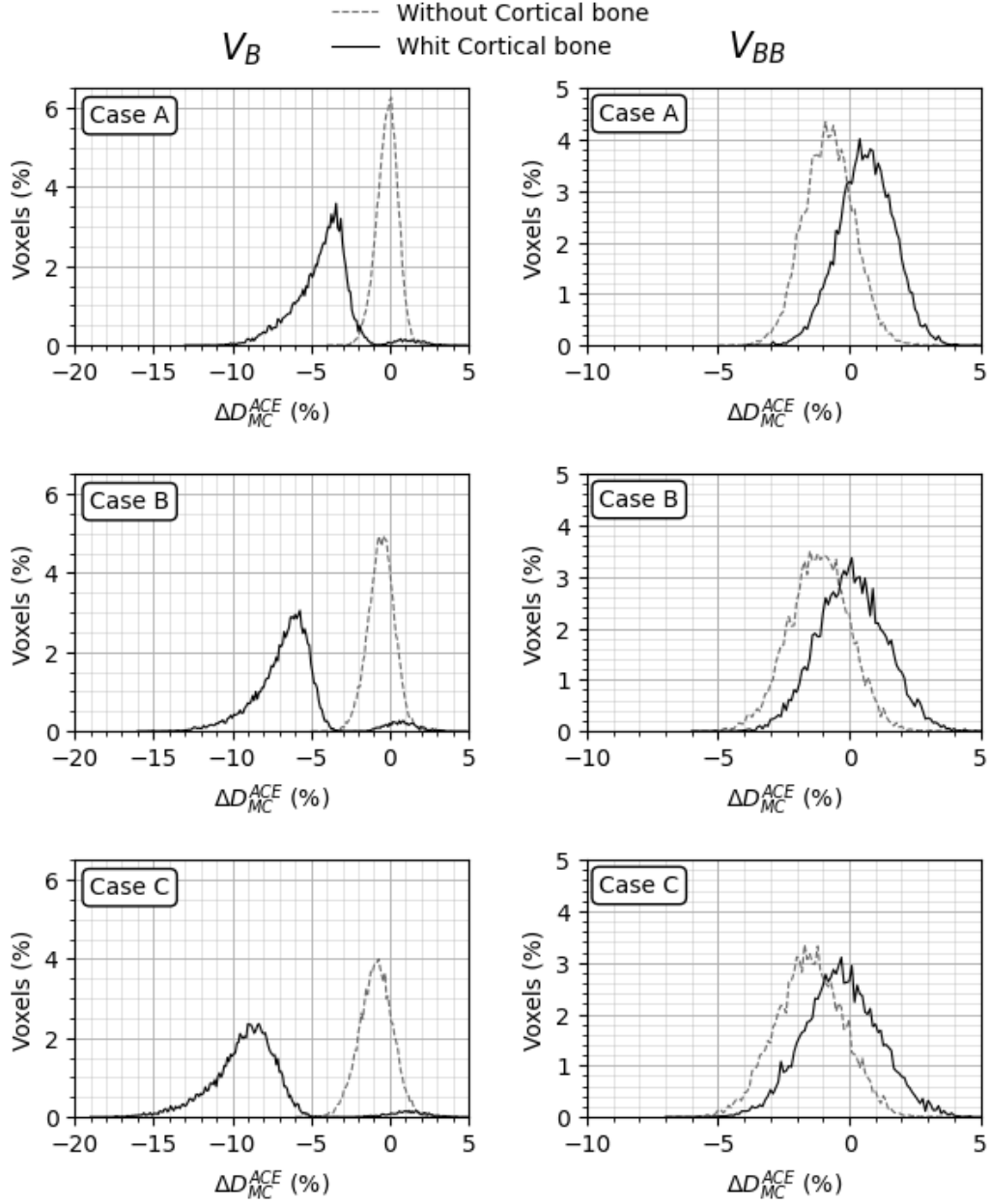Figure 15: Solid lines: histograms of ΔD_{MC}^{ACE} in the bone heterogeneity (V_B, left column) and in the volume V_{BB} (see Figure 7), behind the bone heterogeneity (right column). Dashed lines: represents histograms of ΔD_{MC}^{ACE} in the same volumes, in a homogeneous water case.

As can be seen, TG-43 and MC are in good agreement in the "all water case" (gray lines), whereas ACE mostly underestimates the dose (down to approximately 2%).

The effect of the cortical bone heterogeneity can be seen by observing $D^{MC}(z)/D^{TG43}(z)$ through the heterogeneity (black dotted lines). The cortical bone caused a relative dose increase of $D_{m,m}$ (i.e. $D^{MC}(z)$) as compared to the dose to water in water $D_{w,w}$ (i.e. $D^{TG43}(z)$) in the heterogeneity and a dose reduction of about 10% behind the heterogeneity. The relative dose increase was the greatest in case C, i.e. when the bone was positioned at the largest distance from the source configuration.

It is clear from the profiles that ACE fails in predicting the the relative dose increase of $D_{m,m}$ in the heterogeneity. Both $D^{MC}(z)/D^{TG43}(z)$ and $D^{ACE}(z)/D^{TG43}(z)$ yield negative gradients in the cortical bone heterogeneity.

Table 7 present the mean dose to the three volumes V_B, V_{BB} and V_{IFB} (see Figure 7), as determined from $D^{MC}(\mathbf{r})$ ($\overline{D}_{V_x}^{MC}$), from $D^{TG43}(\mathbf{r})$ ($\overline{D}_{V_x}^{TG43}$), and from $D^{ACE}(\mathbf{r})$ ($\overline{D}_{V_x}^{ACE}$), respectively. As the prescribed dose was set to 1 Gy, the mean doses can be viewed either as the absolute dose in units cGy or as the percentage of the prescribed dose.

Table 7: The mean relative statistical uncertainty ($\overline{\sigma}$) in the MC calculated dose distribution, and the mean dose as calculated from the MC ($\overline{D}^{MC}$), TG-43 ($\overline{D}^{TG43}$) and ACE ($\overline{D}^{ACE}$) calculated dose distribution, respectively, in the three volumes V_B, V_{BB} and V_{IFB} defined in section 3.4, Figure 7. Column 7 and 8 gives the ratios $\overline{D}_{V_x}^{TG43}/\overline{D}_{V_x}^{MC} = R_{V_x}^{TG43}$ and $\overline{D}_{V_x}^{ACE}/\overline{D}_{V_x}^{MC} = R_{V_x}^{ACE}$, respectively.

Case	Distance to bone[a]	$\overline{D}^{MC}$ (cGy)	$\overline{\sigma}$ (%)	$\overline{D}^{TG43}$ (cGy)	$\overline{D}^{ACE}$ (cGy)	R^{TG43} (%)	R^{ACE} (%)
		Mean Dose in volume V_B					
A	2 cm	45.1	0.6	44.8	43.4	99	96
B	3 cm	26.2	0.7	25.1	24.6	96	94
C	4 cm	17.3	0.9	16.0	15.8	92	91
		Mean Dose in volume V_{BB}					
A	2 cm	15.6	0.9	17.3	15.7	111	101
B	3 cm	10.6	1.1	11.8	10.6	111	100
C	4 cm	7.7	1.2	8.5	7.66	110	100
		Mean Dose in volume V_{IFB}					
A	2 cm	92.6	0.4	92.4	93.2	100	101
B	3 cm	43.4	0.6	43.3	43.5	100	100
C	4 cm	25.0	0.7	24.9	25.0	100	100

[a]The distance along the z axis from the origin to the the first voxel containing bone.
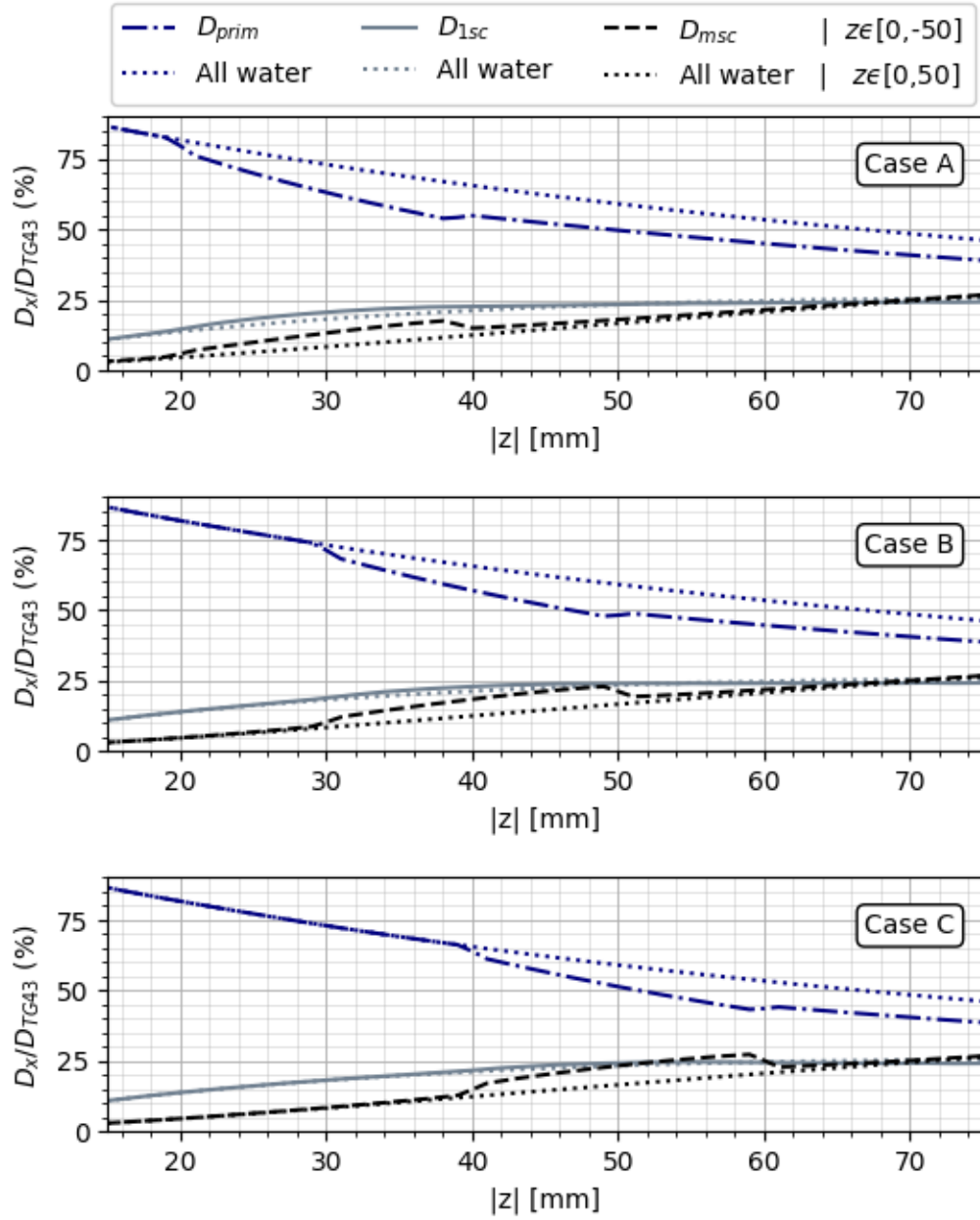
Figure 16: The three components D_{prim}, D_{1sc} and D_{msc} of the $D^{ACE}(z)$ profile from the right column Figure 14, normalized to the dose as calculated with TG-43 and plotted as a function of the absolute distance to the origin.

Column 7 and 8 of Table 7 gives the ratios $\overline{D}_{V_x}^{TG43}/\overline{D}_{V_x}^{MC}=R_{V_x}^{TG43}$ and $\overline{D}_{V_x}^{ACE}/\overline{D}_{V_x}^{MC}=R_{V_x}^{ACE}$, respectively. In volume V_B both ratios are less than 100% for all cases, indicating that both TG-43 and ACE underestimated the mean dose to the cortical bone. The magnitude of the underestimation increased as the bone was positioned farther away from the source configuration (e.g. $R_{V_B}^{ACE}$ equals 96% in case A and 91% in case C) and was always greater for ACE than for TG-43 (e.g. in case A, $R_{V_B}^{TG43} = 99\%$ whereas $R_{V_B}^{ACE} = 96\%$).

In volume V_{BB}, $R_{V_{BB}}^{TG43} \approx 111\%$ for all cases, which means that TG-43 overestimated the mean dose behind the cortical bone with about 11%. ACE and MC yielded similar estimates of the mean dose to V_{BB}. The highest deviation was found in case A where $\overline{D}_{V_{BB}}^{MC} = 15.6$ cGy and $\overline{D}_{V_{BB}}^{ACE} = 15.7$ cGy, hence $R_{V_{BB}}^{TG43} \approx 101\%$.

Both ACE and TG-43 were able to predict the mean dose to V_{IFB}, i.e. the effect of the cortical bone heterogeneity on the dose distribution directly in front of the bone was negligible.

The three components (D_{prim}, D_{1sc} and D_{msc}) from the dose profiles $D^{ACE}(z)$ in the right column of Figure 14 has been plotted in Figure 16. All components are normalised to $D^{TG43}(z)$, and are plotted as a function of the absolute distance from the origin. Recall that negative values of z represents the profiles with the heterogeneity and positive values of z are taken as representatives of the profiles in an all water cases.

In summation, the bone heterogeneity caused a dose reduction in D_{prim}, a small but discernible dose increase in D_{1sc}, and a dose increase in D_{msc}.

5. Discussion

As described in section 2.2.1, the collapsed cone superposition algorithm utilizes the collapsed cone approximation, which gives rise to discretization artifacts. The severeness of these artifacts has been found to decrease in multiple-source configurations [7, 20]. This was also shown in this study. The explanation is thought to be a combination of the conclusions made by Carlsson Tedgren and Ahnesjö [20]: that the artifacts decrease as a result of decreased fluence gradients in multiple-source configurations, and by Ma et al. [7]: that the discretization artifacts from different dwell positions superimpose and "blurr" each other out.

However, when the number of dwell positions were increased from 5 to 21 in the line implant (i.e. the distance between dwell positions were decreased from 5 mm to 1 mm) the accuracy of ACE was not improved. This may be a result of the above mentioned processes counteracting each other, as decreasing the distance between dwell positions also increased the dose (and therefore also the fluence) gradients (see Figure 10). Hence, as more dwell positions were added to the 2 cm long line implant, the auspicious effect of blurring the artifacts dominated up to a certain limit, after which the opposing effect of the gradients prevented further improvement and slightly worsened the result.

In patient cases, the distance between dwell positions are seldom less than 5 mm and they are usually not positioned in as symmetric geometries. Symmetrical line and area implants may be utilized in e.g. lip or skin treatments, but are then bent to fit the patient anatomy and treatment site. Unsymmetrical source configuration may favor the "blurring effect" as artifacts from different dwell positions then occur in a more random manner. Therefore, the above situation is unlikely to be observed in clinical practice and it is well

motivated to reduce the number of transport lines as the number of dwell positions are increased, as is the case in ACE.

The result of this study also showed that the majority of overestimations over 2% (taking TG-43 dosimetry as the truth) made by ACE in the ray-like structures, created by the collapsed cone approximation, were found at dose levels of $\leq 5\%$ of the prescribed dose. In general, ACE underestimated the dose as compared to TG-43. The most probable value of ΔD_{TG43}^{ACE} were, for all combinations of dwell positions, less than zero, which was also the case in the study by Ma et al. [7].

It has been shown by Carlsson Tedgren et al. that the multiple-scattered dose component depend on the relationship between the phantom size utilized in the generation of multiple-scattered dose kernels and the size of the phantom/patient in which the dose is to be calculated [10]. If the dimensions of the phantom in which the multiple-scattered dose kernel has been generated is smaller than the phantom/patient in which the dose is to be calculated, an underestimation can be expected. The magnitude of the underestimation increase with an increased distance from the source location. In the reverse conditions, the opposite would occur. Hence, as the phantom utilized in the study of the discretization artifacts was relatively large (505^3 mm^3), to ensure TG-43 conditions, an underestimation was expected. Whether or not ACE would underestimate the dose in a real patient case would therefore be dependent on the patient size, and can hence not be judged from this study. Further studies, utilizing real patient cases and treatment locations at which MB-DCAs may be preferable over TG-43, should be performed to answer the question if the current multiple-scattered kernel in use is generated in a phantom of optimal dimensions. If a large difference is observed between different treatment sites, it may be motivated to utilize multiple-scattered kernels derived in phantoms of different dimensions for different treatment locations.

From the color plots in Figure 8 and the 2D histograms in Figure 11 it is clear that the performance of ACE is highly dependent on the resolution of the calculation grid. As the voxel size in the calculation grid is increased, the local dose difference ratio is decreased. As can be seen in the 2D histograms in Figure 11, underestimations below -4%, in the z=0 plane, for the three line implants only occurred outside the second calculation box and hence for doses of less than 2% of the prescribed dose. Therefore, the underestimations can be expected to be clinically irrelevant for the line implants. For the cube implants, the 5% isodose lines are located closer to the edges of the second calculation box. Hence, especially when brachytherapy treatments are used as a boost to EBT, the underestimations made by ACE may become significant. It is therefore important that the user is aware of the ACE's calculation grid and its effects, so that the higher accuracy level, with larger first- and second calculation boxes (see section 1), is chosen whenever relevant dose levels are located at a distance of 8 cm or more from the closest dwell position.

In the investigation of ACE's behavior in cortical bone, the MC platform ALGEBRA was used as a reference. Hence, in the following discussion, the MC calculated dose will be viewed as the truth.

It should be mentioned that the case of a cortical bone heterogeneity with uniform density assignment, as in this study, may be viewed as an extreme case. In a more realistic patient case, with CT derived densities, the overall density of bone is expected to be lower than 1.92 g/cm^3. To utilize CT derived densities and uniform tissue compositions is the current recommendation of the AAPM TG-186 [19]. The uniform density assignment

method was chosen in this study to enhance the behavior of ACE in non-water media and search for general algorithm behavior.

The results of the study of ACE's performance in cortical bone was in agreement with previous studies (see e.g. the study by Ma et al. [7]), i.e. ACE underestimated the dose to cortical bone (see Figure 14). ACE underestimated the mean dose to the bone heterogeneity with -4% to -9% (see Table 7). Utilizing the TG-43 formalism, i.e. neglecting the effects of the bone heterogeneity, gave slightly better results in all three cases (see Table 7). The largest deviation between ACE and TG-43 was observed in case A (i.e. with the cortical bone positioned closest to the source configuration) where the mean dose to the cortical bone heterogeneity was underestimated with 4% and 1%, respectively.

The underestimations seen in ACE became worse when the heterogeneity was positioned farther away from the source configuration, indicating that the error made in ACE is mainly located in the first- or multiple-scattered dose calculation.

Behind the bone heterogeneity, as viewed by the source configuration, TG-43 overestimated the dose by about 10% (see Figure 14), whereas ACE was successful in estimating the dose reduction behind the heterogeneity. The mean dose, as calculated with ACE and MC, respectively, to a volume of 3x3x1 cm^3 located directly behind the bone heterogeneity agreed within 1%. However, an increased amount of dose overestimations in the ACE calculated dose distribution, as compared to the performance of ACE in an all water case, was observed in this region for all three cases (see the histograms in Figure 15). Overestimations behind cortical bone heterogeneities has also been observed by Ma et al. [7]. These overestimations, in combination with the underestimations in the heterogeneity, may be caused by a dose displacement in the ACE algorithm.

When utilizing the TG-43 formalism it is well known that the reported dose is $D_{\mathrm{w,w}}$. Hence, if the question arise whether or not a heterogeneity will cause a significant change in the dose distribution, it can be evaluated by an experienced physicist and action, such as using an MBDCA, bolus, or else, can be taken if necessary. If an MBDCA is to be used, one would assume heterogeneities are taken into account and the reported dose is $D_{\mathrm{m,m}}$, alternatively $D_{\mathrm{w,m}}$, with acceptable accuracy. Furthermore, MBDCAs are more time consuming and may hence only be used when the limitations in the TG-43 formalism are expected to be significant. As, in contrast to TG-43, a deeper understanding of the specific algorithm is needed to predict when an MBDCA will fail, and how/how much it will affect the dose distribution, MBDCA calculated dose distributions may be erroneously taken as the true dose distribution in clinical evaluations. Therefore, before ACE is used on routine in clinical practice, the origin of the error seen in ACE when a cortical bone heterogeneity is present should be identified, so that the algorithms limitations are well known, or better, so that a solution to the problem can be found. Below follows a discussion that aims to provide a hypothesis of why the error in ACE occur, and suggest solutions, left to be proven in future studies.

To locate the origin of the underestimation in cortical bone made by ACE, the dose profiles divided into its' three constituents D_{prim}, D_{1sc} and D_{msc} (see Figure 16) could be viewed. Unfortunately, the version of ALGEBRA available for this project did not allow for the dose components to be scored separately. Therefore, it is not possible to locate the error in ACE to a specific dose component solely from the results of this study. However, as stated earlier, the study indicated that the error in ACE is located in one of the scatter dose components and that the error leads to a displacement of dose. From these results, in

combination with discussing the expected behavior of the three dose components, studying the assumptions made in the collapsed cone algorithm in brachytherapy and looking at previous studies, a hypothesis has been formed.

The behavior of the three components of ACE (see Figure 16) has been analyzed with the help of analytically calculated monoenergetic dose profiles that can be found in appendix C. For the primary dose component, no "new" energy is released along a ray. Hence, an increased gradient can be seen in D_{prim} through the cortical bone heterogeneity, caused by the higher attenuation coefficient of cortical bone relative water. For photons above 200 keV, $(\mu_{\text{en}}/\mu)_{\text{cortical bone}}/(\mu_{\text{en}}/\mu)_{\text{water}} < 1$. Hence, as illustrated in Figure 19 in appendix C, $D_{\text{m,m}}$ is less than the $D_{\text{w,m}}$. As the weighted average photon energy of an ^{192}Ir source is approximately equal to 400 keV, a reduction of D_{prim} in and behind the cortical bone heterogeneity was expected [14].

As "new" energy is released along a transport line in the scatter dose calculations, and the energy available for first- and multiple-scattered photons depend on previous photon generations, it is more difficult to predict the effect of the cortical bone heterogeneity on the scattered dose. However, the relative dose increase observed in D_{1sc} and D_{msc} in Figure 16 are thought to be caused by photons of an energy below 200 keV, as for these photons $(\mu_{\text{en}}/\rho)_{\text{cortical bone}}/(\mu_{\text{en}}/\rho)_{\text{water}} > 1$. Hence, for a monoenergetic point source with an energy of 200 keV or less, a relative dose increase between $D_{\text{m,m}}$ and $D_{\text{w,w}}$ occur in the proximal part (as viewed from the source) of a cortical bone heterogeneity (see appendix C). The higher the ratio, the higher the relative dose increase. Also, the depth of where $D_{\text{m,m}}$ equals $D_{\text{w,w}}$ increase as the ratio is increased.

As can be seen in Figure 4 in the study by Papagiannis et al., the energy distribution of scattered photons from a ^{192}Ir point source include a significant fraction of photons below 200 keV [8]. A large fraction of these low energy photons can be expected to be multiple-scattered photons. As the ratio of mass absorption coefficient between cortical bone and water increase as the energy decrease from 200 keV to 70 keV (see Figure 20 in appendix C), the highest relative dose increase may be expected to be found in D_{msc}, which was also the case. However, as the effect of the increased attenuation in cortical bone is an increased energy release, and the increased absorption in cortical bone cause a decreased fraction of the energy released to be passed on to the next scatter generation, the magnitude of the dose increase is hard to predict. But, by noting that the dose to cortical bone for photons of an energy below 200 keV is highly dependent on the high ratio of absorption coefficients of cortical bone and water (see Appendix C) and realizing that no scaling of absorption coefficients are utilized in the heterogeneity scaling of the multiple-scattered dose kernel, the multiple-scattered dose in cortical bone is thought to be underestimated. Hence, the error made in ACE is most probably located in the multiple-scattered dose calculation. This is also the indication in the study by Terribilini et al. where the multiple-scattered dose to the ribs were underestimated in a HDR ^{192}Ir treatment of breast cancer [11]. To confirm the location of the error in ACE, a newer version of ALGEBRA, which can score the dose components separately, should be utilized.

A hypothesis is that the errors seen in ACE mainly are caused by an invalid assumption in the heterogeneity scaling of the multiple-scattered dose kernel. To understand the assumption, assume a kernel for each scatter generation exists. The volume integral over an infinite volume of the first-scattered dose kernel equals the fraction of energy to be deposited as first-scattered dose, that is $B/b \approx \mu_{\text{en, 1sc}}/\mu_{\text{1sc}}$. The volume integral of a second-scattered

dose kernel should equal the fraction of energy to be deposited as second-scattered dose ($\mu_{en,\,2sc}/\mu_{2sc}$), the volume integral of a third-scattered dose kernel should equal the fraction of energy to be deposited as third-scattered dose ($\mu_{en,\,2sc}/\mu_{2sc}$), and so on. Hence, heterogeneity scaling should consider the difference in attenuation and absorption coefficients between water and non-water media.

However, for practical reasons, a separate dose kernel for each scatter generation is not utilized in ACE, and all scatter generations of order 2 or higher are merged into the multiple-scattered kernel [15]. When scaling the multiple-scattered kernel for non-water media, only differences in attenuation coefficients are considered, as energy balance requires that all energy available for the multiple-scattered generation has to be deposited as multiple-scattered dose (i.e. $\mu_{en,\,msc}/\mu_{msc} = 1$). Therefore, ACE assumes that any generation specific variations in μ_{en}/μ for a media and water can be neglected for photons scattered more than once. This approach might fail to correct for an increased absorption close to the point of scatter release in bone, as compared to water, caused by an increased amount of photoelectric interactions. This would cause a displacement of dose, and hence also explain the overestimations behind cortical bone heterogeneities, as observed in this study and in the study by Ma et al. [7]. In the example above of generation specific kernels, the effect would be accounted for by the use of absorption coefficient ratios.

If the hypothesis is correct, the opposite effect could be expected in air, i.e. overestimations in ACE calculated dose distributions as a consequence of the neglected effect of a decreased absorption ratio close to the point of scatter release in air as compared to water. Overestimations of the dose to air has been observed in the study by Abe et al. [40], and is visible on the isodose lines in Figure 4 in the study by Terribilini et al. [11]. However, systematic studies in which the local dose difference ratio in a volume of air is compared to the local dose difference ratio in the same volume, at the same location, in an all water case is necessary to separate the effect from other factors affecting the performance of ACE.

Given that the hypothesis is correct, a solution to the problem may be to use media specific multiple-scattered dose kernels whenever the absorption ratio for multiple-scattered photons differ significantly form that of water and switch to these kernels when encountering the non-water media. This method was introduced by Carlsson Tedgeren and Ahnesjö for the material lead [2]. However, if utilizing Hounsfield Units to define the properties of a material, the kernel specific approach can be impractical for organic tissues which are not as well defined as lead. Also, if ACE is to be for lower energy sources in the future, the number of material specific kernels needed would increase.

A new suggested solution to the problem seen in ACE is to derive new "effective" attenuation scaling factors, since an increased absorption effectively means a reduction of the number of photons available for higher scatter generations [12]. The detailed design of such scaling factors are left for future work and whether they are able to improve the accuracy of ACE in non-water media remains to be proven thought future computational experiments. A demonstration of the idea can be found in appendix D.

6. Conclusions

In this work, the MBDCA ACE, by Elekta, has been investigated with the aims (1) to study how the discretization artifact, associated with the collapsed cone approximation, depend on the number of dwell positions and (2) to form a hypothesis with an explanation and solution to the reported dose underestimations in bone previously observed in ACE [7–9].

It has been shown in previous studies that the severeness of the discretization artifacts decreased in multiple-source configurations [7, 20]. This finding was confirmed by the current study. However, the results revealed that increasing the number of dwell positions does not guarantee a reduction of the artifacts, if dwell positions are added in a way that also increases the fluence gradients. The finding is thought to have little clinical relevance as increasing the number of dwell positions in a more unsymmetrical manner than done in this study is thought to seldom result in a worsening of the artifacts.

The majority of dose overestimations above 4% in the ray like artifacts were located outside the 5% isodose line. In general ACE underestimated the dose. The majority of local dose difference ratios below -4% were observed at a distance of ≥ 8 cm from the closest dwell position. At these distances the dose levels can be expected to be low ($< 5\%$ of the prescribed dose) and the clinical relevance depend on the specific treatment location and whether brachytherapy is used together with EBT or not.

ACE showed to be unsuccessful in predicting the dose to cortical bone but successful in accounting for the dose reduction behind the heterogeneity. ACE underestimated the mean dose to the heterogeneity with $\geq 4\%$, depending on the location of the heterogeneity, whereas utilizing the TG-43 formalism gave slightly better results (1-3% closer to MC than ACE), especially at high dose levels. Hence, ACE should be used with caution when a cortical bone is an OAR, as long as the problem remains.

The results showed that the magnitude of the underestimation to cortical bone made by ACE increased as the heterogeneity was positioned farther away from the source configuration and that the heterogeneity caused a small increase in the number of positive local dose difference ratios directly behind the heterogeneity. This indicates that the error in ACE is located in one of the scattered-dose components and that the ACE algorithm caused a displacement of dose. The error is thought to be located in the multiple-scattered dose component, which was also the case in the study by Terribilini et al. [11]. A hypothesis is that the errors seen in ACE are caused by the neglected effect of media specific absorption coefficients in the multiple-scattered dose kernel, which may result in a dose underestimation close to the point of energy release (kernel origin) in cortical bone. A suggested solution to the problem, formed in this project, is to utilize effective attenuation scaling factors [12]. However, the detailed design of such scaling factors, and whether they are able to solve the problem remains to be proven in future work.

Bibliography

[1] M. J. Rivard et al. "Update of AAPM Task Group No. 43 Report: A revised AAPM protocol for brachytherapy dose calculations". In: *Medical physics* 31.3 (2004), pp. 633–674.

[2] Å. K. Carlsson Tedgren and A. Ahnesjö. "Accounting for high Z shields in brachytherapy using collapsed cone superposition for scatter dose calculation". In: *Medical Physics* 30.8 (2003), pp. 2206–2217.

[3] M.J. Rivard, J.LM. Venselaar, and L. Beaulieu. "The evolution of brachytherapy treatment planning". In: *Medical physics* 36.6Part1 (2009), pp. 2136–2153.

[4] L. Beaulie, Y. Ma, and B. van Veelen. *ACE - Advanced Collapsed Cone Engine.* Art. nr. 888.00638. Elekta White Paper, 2014. Avalible at: https://www.elekta.com.

[5] A. Ahnesjö. "Collapsed cone convolution of radiant energy for photon dose calculation in heterogeneous media". In: *Medical physics* 16.4 (1989), pp. 577–592.

[6] A. Ahnesjö, B. van Veelen, and Å Carlsson Tedgren. "Collapsed cone dose calculations for heterogeneous tissues in brachytherapy using primary and scatter separation source data". In: *Computer methods and programs in biomedicine* 139 (2017), pp. 17–29.

[7] Y. Ma et al. "Validation of the Oncentra Brachy Advanced Collapsed cone Engine for a commercial 192Ir source using heterogeneous geometries". In: *Brachytherapy* 14.6 (2015), pp. 939–952.

[8] P. Papagiannis, E. Pantelis, and P. Karaiskos. "Current state of the art brachytherapy treatment planning dosimetry algorithms". In: *The British journal of radiology* 87.1041 (2014), p. 20140163.

[9] V. Peppa et al. "A user-oriented procedure for the commissioning and quality assurance testing of treatment planning system dosimetry in high-dose-rate brachytherapy". In: *Brachytherapy* 15.2 (2016), pp. 252–262.

[10] Å. Carlsson Tedgren, M. Plamondon, and L. Beaulieu. "The collapsed cone algorithm for 192Ir dosimetry using phantom-size adaptive multiple-scatter point kernels". In: *Physics in Medicine & Biology* 60.13 (2015), p. 5313.

[11] D. Terribilini et al. "Performance evaluation of a collapsed cone dose calculation algorithm for HDR Ir-192 of APBI treatments". In: *Medical physics* 44.10 (2017), pp. 5475–5485.

[12] A. Ahnesjö. Professor at Department of Immunology, Genetics and Pathology, Medical Radiation Sciences, Uppsala University. Personal communication. May 2021.

[13] C. Chargari et al. "Brachytherapy: An overview for clinicians". In: *CA: a cancer journal for clinicians* 69.5 (2019), pp. 386–401.

[14] P. Mayles, A. Nahum, and J-C. Rosenwald. *Handbook of radiotherapy physics: theory and practice.* Chapter 51, pages 1101-1115. Taylor Francis Group, CRC Press, New York: 2007.

[15] Å. K. Carlsson and A. Ahnesjö. "The collapsed cone superposition algorithm applied to scatter dose calculations in brachytherapy". In: *Medical physics* 27.10 (2000), pp. 2320–2332.

[16] R. Nath et al. "Dosimetry of interstitial brachytherapy sources: recommendations of the AAPM Radiation Therapy Committee Task Group No. 43". In: *Medical physics* 22.2 (1995), pp. 209–234.

[17] M. J Rivard et al. "Supplement to the 2004 update of the AAPM Task Group No. 43 Report". In: *Medical physics* 34.6Part1 (2007), pp. 2187–2205.

[18] J. Perez-Calatayud et al. "Dose Calculation for Photon-Emitting Brachytherapy Sources with Average Energy Higher than 50 keV: Full Report of the AAPM and ESTRO". In: *Medical physics* 39.5 (2012), pp. 2904–2929.

[19] L. Beaulieu et al. "Report of the Task Group 186 on model-based dose calculation methods in brachytherapy beyond the TG-43 formalism: current status and recommendations for clinical implementation". In: *Medical physics* 39.10 (2012), pp. 6208–6236.

[20] Å. Carlsson Tedgren and A. Ahnesjö. "Optimization of the computational efficiency of a 3D, collapsed cone dose calculation algorithm for brachytherapy". In: *Medical physics* 35.4 (2008), pp. 1611–1618.

[21] J. Guinot et al. "Efficacy of high-dose-rate interstitial brachytherapy in patients with oral tongue carcinoma". In: *Brachytherapy* 9.3 (2010), pp. 227–234.

[22] A. Gevorgyan et al. "Radiation-induced craniofacial bone growth disturbances". In: *Journal of Craniofacial Surgery* 18.5 (2007), pp. 1001–1007.

[23] S. Nag and D. Tippin. "Brachytherapy for pediatric tumors". In: *Brachytherapy* 2.3 (2003), pp. 131–138.

[24] C. Kirisits et al. "Review of clinical brachytherapy uncertainties: analysis guidelines of GEC-ESTRO and the AAPM". In: *Radiotherapy and oncology* 110.1 (2014), pp. 199–212.

[25] E. Pantelis et al. "The effect of finite patient dimensions and tissue inhomogeneities on dosimetry planning of 192Ir HDR breast brachytherapy: a Monte Carlo dose verification study". In: *International Journal of Radiation Oncology* Biology* Physics* 61.5 (2005), pp. 1596–1602.

[26] G. Anagnostopoulos et al. "The effect of patient inhomogeneities in oesophageal 192Ir HDR brachytherapy: a Monte Carlo and analytical dosimetry study". In: *Physics in Medicine & Biology* 49.12 (2004), p. 2675.

[27] Å. K. Carlsson and A. Ahnesjö. "Point kernels and superposition methods for scatter dose calculations in brachytherapy". In: *Physics in Medicine & Biology* 45.2 (2000), p. 357.

[28] H. Afsharpour et al. "ALGEBRA: ALgorithm for the heterogeneous dosimetry based on GEANT4 for BRAchytherapy". In: *Physics in Medicine & Biology* 57.11 (2012), p. 3273.

[29] Y. Ma et al. "A generic TG-186 shielded applicator for commissioning model-based dose calculation algorithms for high-dose-rate 192Ir brachytherapy". In: *Medical physics* 44.11 (2017), pp. 5961–5976.

[30] F. Ballester et al. "A generic high-dose rate 192Ir brachytherapy source for evaluation of model-based dose calculations beyond the TG-43 formalism". In: *Medical physics* 42.6Part1 (2015), pp. 3048–3062.

[31] M. Persson. *Monte Carlo simulations to re-calculate doses for patients that have undergone ^{192}Ir HDR brachytherapy in the head and neck region.* Master thesis in medical radiation physics at Stockholm University (2013). Unpublished.

[32] J. F. Williamson. "Monte Carlo evaluation of kerma at a point for photon transport problems". In: *Medical physics* 14.4 (1987), pp. 567–576.

[33] C.A Collins Fekete. *ALGEBRA: ALgorithm for the heterogeneous dosimetry based on GEANT4 for BRAchytherapy.* Manual. CHU De Québec Université Laval (2013). Unpublished.

[34] B. Walters, I. Kawrakow, and D. Rogers. "History by history statistical estimators in the BEAM code system". In: *Medical physics* 29.12 (2002), pp. 2745–2752.

[35] Source Registry. Joint AAPM/IROC Houston Registry of Brachytherapy Sources Meeting the AAPM Dosimetric Prerequisites. *irochouston.mdanderson.org.* Accessed on: 2021-02-16. [Online].
Available: http://irochouston.mdanderson.org/RPC/home.htm.

[36] F. Andersson. *Commissioning of a Model-Based Dose Calculation Algorithm in a Brachytherapy Treatment Planning System at the Karolinska University Hospital.* Master thesis in medical radiation physics at Stockholm University (2020). Unpublished.

[37] L. Beaulieu et al. *Commissioning of Model-Based Dose Calculation Algorithms in Brachytherapy: A Joint AAPM, ESTRO, and ABG Report.* AAPM (2020). Unpublished.

[38] R. Holmberg, T. Hinks, and H. MacLean. *github.com.* RaySearch Laboratories AB. Accessed on: 2021-03-17. [Online].
Available: https://github.com/raysearchlabs/dicomutils.

[39] D. White et al. *Tissue substitutes in radiation dosimetry and measurement, the international commission on radiation units and measurements (ICRU) report 44.* ICRU (1989).

[40] K. Abe et al. "Impact of a commercially available model-based dose calculation algorithm on treatment planning of high-dose-rate brachytherapy in patients with cervical cancer". In: *Journal of radiation research* 59.2 (2018), pp. 198–206.

[41] National Institute of Standards and Technology (NIST). X-RAY Mass Attenuation Coefficients. *nist.gov.* Accessed on: 2021-05-12. [Online].
Available: https://physics.nist.gov/PhysRefData/XrayMassCoef/tab4.html.

Appendices

A. Python script to generate ALGEBRA input files

The following python scrips, written in python 3, generates 2 of the 3 input files to run the MC platform ALGEBRA (see section 3.1.2). The input file is a DICOM RP.dcm file and the output files are called *dwells.dat* and *run.conf*.

```python
#!/usr/bin/env python3
import os, sys
import pydicom
import glob
import numpy as np


# ==================================================================
# Configuration
# ==================================================================
os.chdir(sys.argv[1])
RP = pydicom.dcmread(glob.glob("RP*.dcm")[0])

# ==================================================================
# Create dwells.dat file
# ==================================================================

fdwells = open('dwells.dat','w')

for AS in RP.ApplicationSetupSequence:
    for ch in AS.ChannelSequence:
        W0 = ch.FinalCumulativeTimeWeight
        T = ch.ChannelTotalTime
        nPoints = int(len(ch.BrachyControlPointSequence) / 2)

        for i in range(nPoints):
            cp = ch.BrachyControlPointSequence[2 * i]
            w = ch.BrachyControlPointSequence[2*i+1].CumulativeTimeWeight-cp.CumulativeTimeWeight
            p = cp.ControlPoint3DPosition
            P = np.array([p[0], p[1], p[2]])
            if i==0:
                if len(ch.BrachyControlPointSequence) == 2: direction = np.array([0,0,1])
                else:
                    p1 = ch.BrachyControlPointSequence[2 * (i + 1)].ControlPoint3DPosition
                    P1 = np.array([p1[0], p1[1], p1[2]])

                    v = np.array(P1-P)
                    v_hat = v/np.linalg.norm(v)
                    direction = v_hat
```

```python
            else:
                v = P - prev
                v_hat = v/np.linalg.norm(v)
                direction = v_hat
            if direction[2] < 0: direction = -direction

            fdwells.write('%7.4f ' %np.array(p)[0]) #xpos
            fdwells.write('%7.4f ' % np.array(p)[1]) #ypos
            fdwells.write('%7.4f ' % np.array(p)[2]) #zpos
            time = float(T) * w / float(W0)
            fdwells.write('%7.4f ' % time)  # time
            fdwells.write('%7.4f ' % direction[0])  # xrot
            fdwells.write('%7.4f ' % direction[1])  # yrot
            fdwells.write('%7.4f\n' % direction[2])  # zrot

            prev = P

fdwells.close()
# ================================================================
# Create run.conf file
# ================================================================

frun = open('run.conf','w')

# Change parameters
a='''MODEL           MBDCA_WGIr192
NPHOTONS        60000000
AirKermaRate    %.5f
INSERTSEEDS     0
PARAWORLD       NoParallelWorld
''' % (RP.SourceSequence[0].ReferenceAirKermaRate)
frun.write(a)
frun.close()
```

B. Local dose difference ratios in the y & x planes

Figure 17 and 18 below shows the local dose difference ratio (ΔD_{TG43}^{ACE}) obtained in part 1 of the study, in the $y = 0$ and the $x = 0$ plane, respectively. ΔD_{TG43}^{ACE} for the $z = 0$ plane is presented in section 4.1.
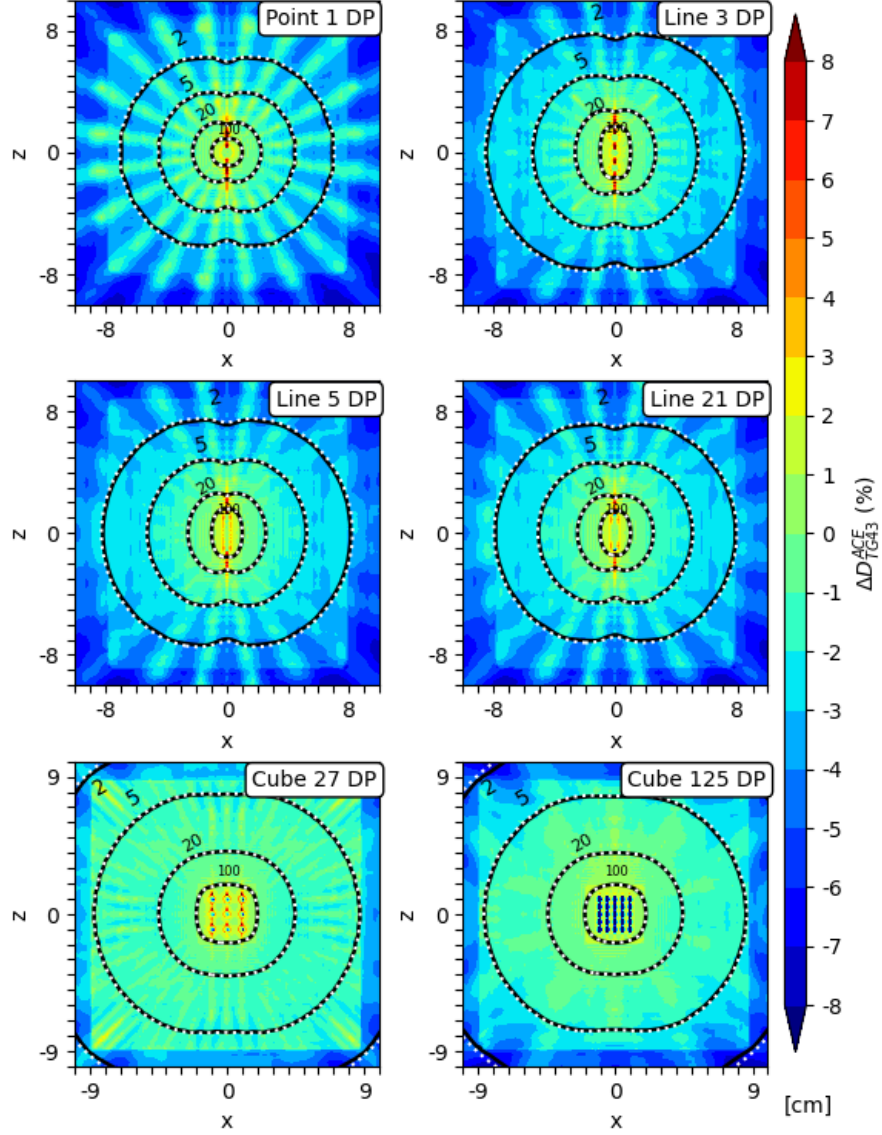

Figure 17: Color plots of ΔD_{TG43}^{ACE} in the $y = 0$ plane for the six cases presented in table 3. The 100%, 20%, 5% and 2% isodose lines from the TG-43 calculated dose distribution (white dots) and ACE calculated dose distribution (black lines) are also presented.
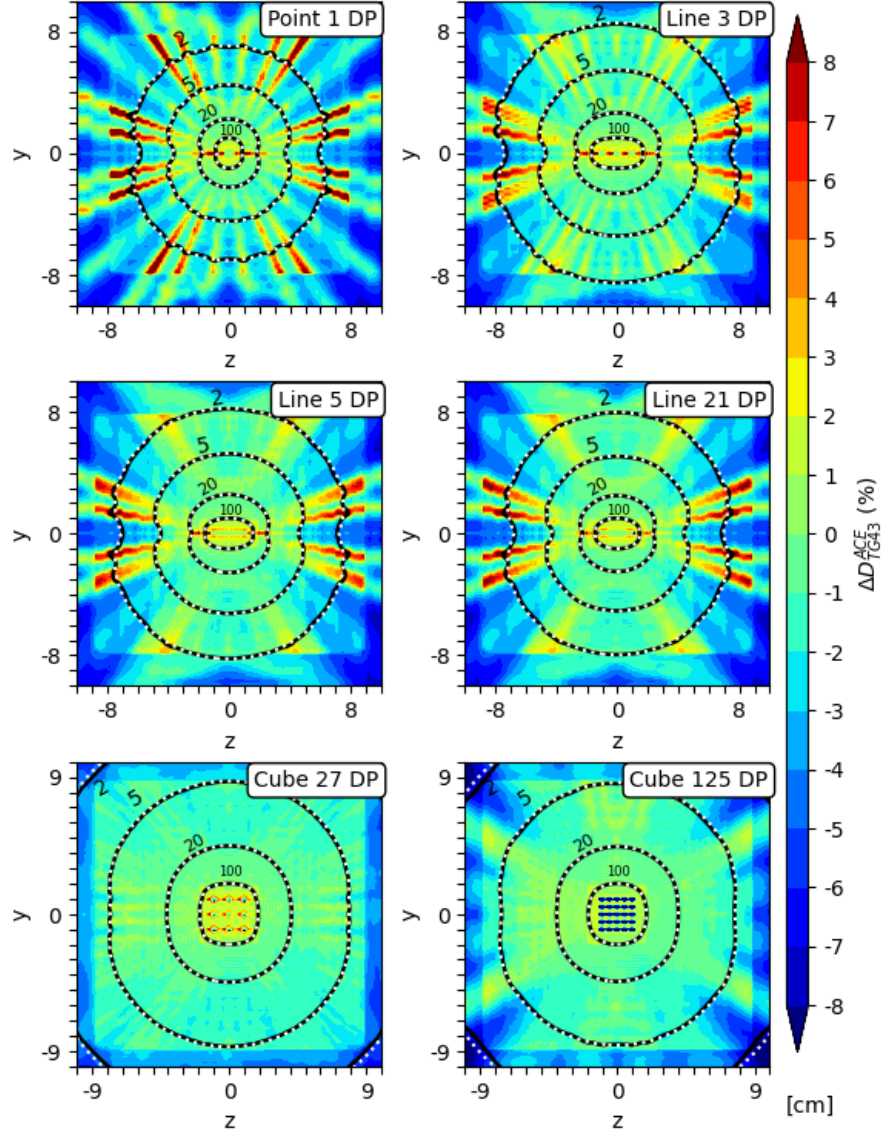
Figure 18: Color plots of ΔD^{ACE}_{TG43} in the $x = 0$ plane for the six cases presented in table 3. The 100%, 20%, 5% and 2% isodose lines from the TG-43 calculated dose distribution (white dots) and ACE calculated dose distribution (black lines) are also presented.

C. Analytical dose profiles & Mass absorption coefficient ratios

To understand how the dose distribution in an homogeneous water phantom is affected by a cortical bone heterogeneity, it can be useful to study the behavior of monoenergetic photon spectra. Hence, the primary dose in a water phantom along a 1D line $r\epsilon[0 \text{ mm}, 59 \text{ mm}]$, with a cortical bone heterogeneity located at $10 \text{ mm} \leq 4 \leq 30 \text{ mm}$, has been calculated analytically for four monoenergetic photon spectra, 100 keV, 150 keV, 200 keV and 400 keV. The analytical dose profiles were calculated as,

$$D(r_i) = \frac{1}{4\pi r_i^2}\Phi(r_{i-1})e^{-\mu_i\Delta r}(\frac{\mu_{\text{en}}}{\rho})_i, \tag{42}$$

where $\Phi(r_i)$ is the energy fluency at location r_i and $\Phi(0)$ was set to 1 J/cm^2. By appropriate choose of the linear attenuation coefficients μ_i and the mass absorption coefficient $(\mu_{\text{en}}/\rho)_i$ (either taken for water or for the material at position r_i), the dose to water in water $D_{\text{w,w}}(r_i)$, the dose to water in media $D_{\text{w,m}}$, and the dose to media in media $D_{\text{m,m}}$ has been obtained. The three profiles $D_{\text{w,w}}$, $D_{\text{w,m}}$ and $D_{\text{m,m}}$ for each monoenergetic photon spectra was plotted as a function of r and normalized to the dose at $r_0 = 0$ mm. The values of the mass attenuation and absorption coefficients where taken from the National Institute of Standards and Technology (NIST), and the mass absorption coefficient ratio for cortical bone and water, and air and water, has been plotted as a function of photon energy [41].
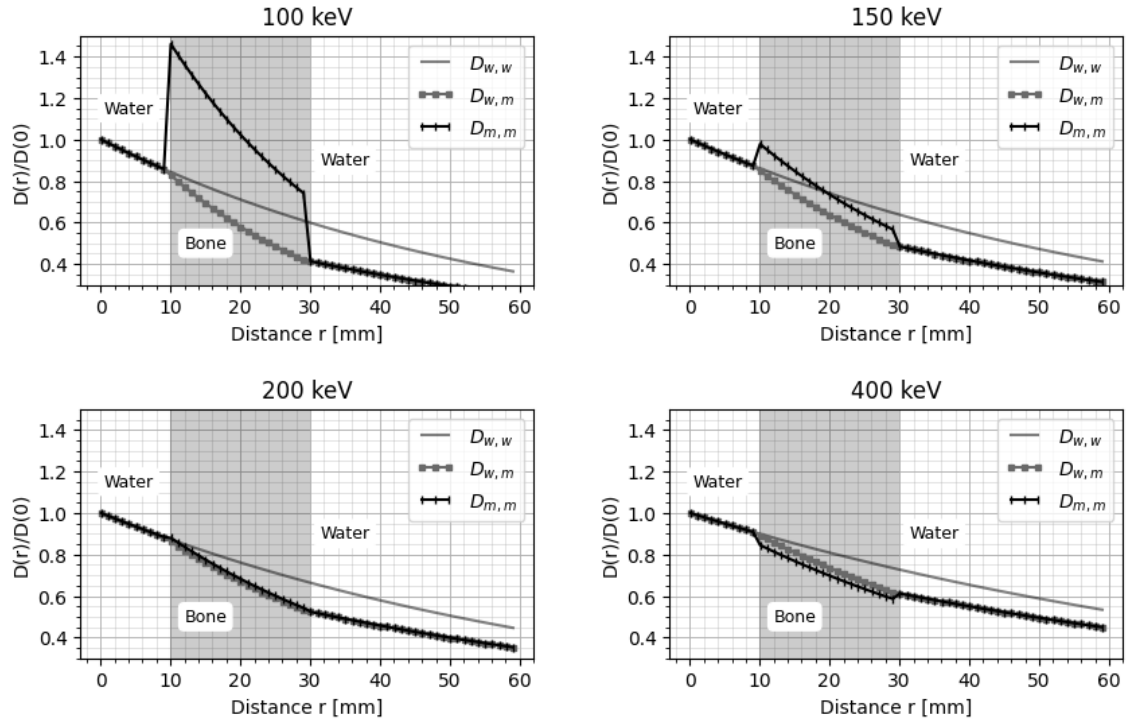

Figure 19: Analytically calculated dose profiles for monoenergetic photon spectra in a water phantom with a cortical bone heterogeneity located at $10 \leq r \leq 30$.

Figure 19 shows the result of the analytically calculated dose profiles for four monoenergetic photon spectra, with ($D_{\mathrm{m,m}}$ and $D_{\mathrm{w,m}}$) and without ($D_{\mathrm{w,w}}$) a cortical bone heterogeneity at $10 \leq r \leq 30$. The ratios of mass absorption coefficients of cortical bone and water, and air and water, as a function of photon energy is presented in Figure 20.

For 400 keV photons $D_{\mathrm{m,m}}$ is less than $D_{\mathrm{w,w}}$ at $r > 10$ mm, and the difference between $D_{\mathrm{m,m}}$ and $D_{\mathrm{w,m}}$ is small, as the difference between mass attenuation coefficients for cortical bone and water is small for photons of an energy above 200 keV (see Figure 20). Hence, the difference between $D_{\mathrm{m,m}}$ and $D_{\mathrm{w,w}}$ are mainly caused by the difference in linear attenuation coefficients.

As the energy decrease from 400 keV to 200 keV the difference in mass attenuation coefficients decrease and, hence, also the difference between $D_{\mathrm{m,m}}$ and $D_{\mathrm{w,m}}$. For photon energies below 200 keV the ratio $(\mu_{\mathrm{en}}/\rho)_{\mathrm{cortical\ bone}}/(\mu_{\mathrm{en}}/\rho)_{water}$ is greater than 1 and vary drastically with energy, as the probability of photoelectric interactions differ significantly between cortical bone and water at lower energies. This cause $D_{\mathrm{m,m}}$ to be greater than $D_{\mathrm{w,m}}$. As can be seen in Figure 19 in the profiles for 150 keV photons, $D_{\mathrm{m,m}}$ is greater than $D_{\mathrm{w,w}}$ in the first 10 mm in the cortical bone heterogeneity before the increased attenuation cause $D_{\mathrm{m,m}}$ to be lower than $D_{\mathrm{w,w}}$. Hence, both the mass absorption and the linear attenuation coefficients highly affect $D_{\mathrm{m,m}}$. As the energy decrease further, the mass absorption coefficient ratio increase drastically (see Figure 20) which cause $D_{\mathrm{m,m}}$ to be much greater than $D_{\mathrm{w,w}}$ and $D_{\mathrm{m,w}}$ at all locations in the cortical bone.
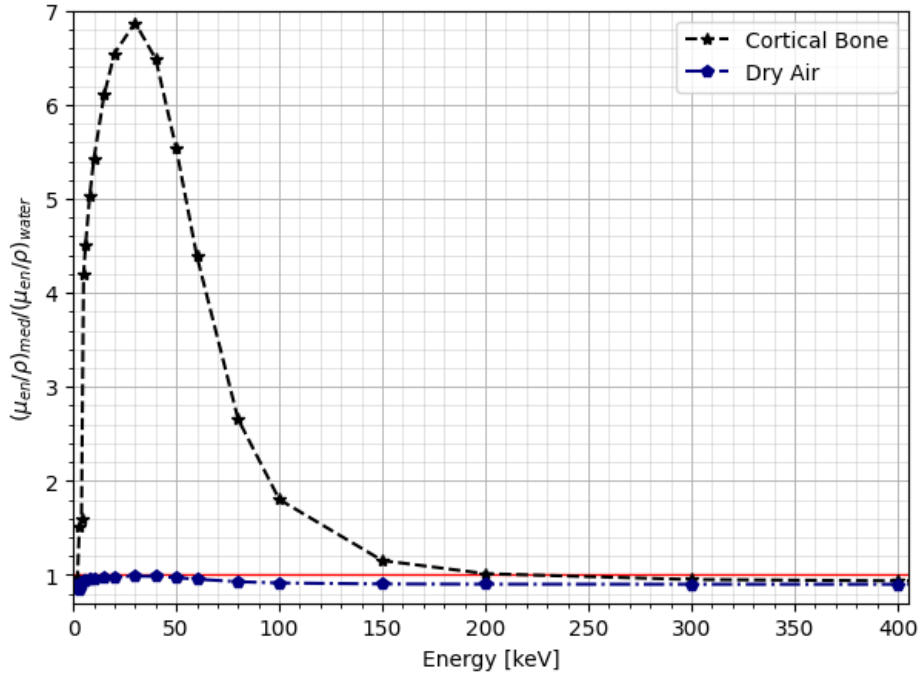

Figure 20: Mass absorption coefficient ratios of cortical bone and water (black stars) and dry air and water (blue diamonds).

D. Motivation of suggested solution

To understand the effect of the multiple-scatter attenuation scaling factor η_{msc}, and motivate the suggested solution of utilizing an "effective" attenuation scaling factor to account for an increase/decrease in energy absorption close to the kernel center in non-water media, a simple illustration is presented below. The nomenclature and equations introduced in section 2.2.4 will here be utilized without further explanation.

Presume we have a single transport line m, that passes through a set of voxels such that the step length Δl_i needed to transverse each voxel i is equal to one another, and equal to $\Delta l_{\max} = 1$ mm. The voxel dimensions are 1^3 mm^3, and the energy released to multiple-scatters photons per unit mass ($S_{2\mathrm{sc}}$) is 1 Gy in each voxel. The transport line is illustrated in Figure 21. Further, assume the kernel coefficients C and c in the multiple-scatter kernel and the solid angles $\Delta\Omega$ are equal to 1 at all locations along m.
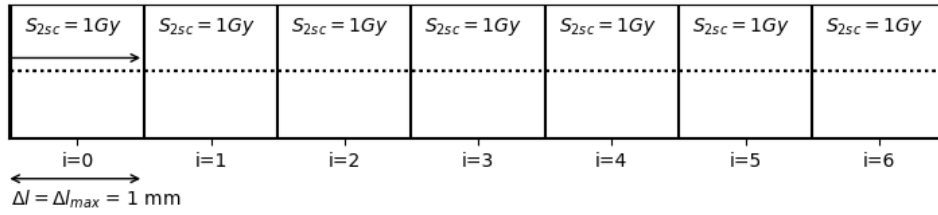

Figure 21: Illustration of a transport line (dotted line) through a set of voxels i. The step length needed to transverse each voxel is 1 mm and $S_{2\mathrm{sc}}$ in each voxel is 1 Gy.

In the multiple-scattered dose calculation, the dose is calculated in 2 steps as explained in section 2.2.4. First $D_{C,i}$ is calculated with the kernel parameters C and c, and then $D_{D,i}$ is calculated from kernel parameters D and d. The final dose to voxel i is then calculated as $D_i = D_{C,i} + D_{D,i}$. In the illustration, only $D_{C,i}$ has been calculated.

For each step i along the transport line in Figure 21, the energy transport and dose deposition has been calculated as [6],

$$\sigma_i = S\rho_i\Delta\Omega\frac{C}{c}, \tag{43}$$

$$\Delta\hat{R}_i = \frac{\sigma_i}{c\,\eta_{\mathrm{msc},i}}\left(1 - e^{-\eta_{\mathrm{msc},i}\,c\,\Delta l}\right), \tag{44}$$

$$\bar{c}_i = \frac{\bar{c}_{i-1}\hat{R}_{i-1} + c\Delta\hat{R}_i}{\hat{R}_{i-1} + \Delta\hat{R}_i}, \tag{45}$$

$$\varepsilon_i = e^{-\eta_{\mathrm{msc},i}\,\bar{c}_i\,\Delta l}, \tag{46}$$

$$D_i = \frac{1}{\Delta l_{\max}\rho_i}((1 - \epsilon_i)\hat{R}_i + (\sigma_i\Delta_l - \Delta\hat{R}_i), \tag{47}$$

$$\hat{R}_i = \varepsilon_i\hat{R}_{i-1} + \Delta\hat{R}_i, \tag{48}$$

with $\hat{R}_i$ and $\bar{c}_i$ set to 0 for $i = 0$. The equations has been explained in section 2.2.4, with the exception of $\bar{c}$ which is a moving average of c_i [6].

Voxels located at a distance of 2-5 cm (i.e. iteration steps 20 to 50) from the beginning of the transport line has been assigned either the density of cortical bone (1.92 g/cm^3) or the density of dry air (0.001225 g/cm^3) and the remaining voxels were assigned the approximate density of water (1 g/cm^3). The energy spectra of multiple-scattered photons were taken as monoenergetic and the attenuation scaling factors $\eta_{\text{msc},i}$ in cortical bone/air were either calculated with the current formula,

$$\eta_{\text{msc},i} = \frac{\mu_{\text{med}}}{\mu_{\text{water}}} \tag{49}$$

or with an hypothetical formula of an effective attenuation scaling factor,

$$\eta_{\text{msc},i} = \frac{\mu_{\text{med}}}{\mu_{\text{water}}} \times \frac{(\mu_{\text{en}}/\rho)_{\text{med}}}{(\mu_{\text{en}}/\rho)_{\text{water}}}. \tag{50}$$

The later, "effective" scaling factor has just been chosen to show the effect of an increased/decreased attenuation scaling factor and lac derivation and motivation. The detailed design of an effective scaling factor is left to be derived in future work.

The python script used in the iteration process is given in Figure 22.

The results are presented in Figures 23 and 24. When the effective attenuation scaling factor is greater than the current attenuation scaling factor, as in cortical bone for photons at 50 and 100 keV, the dose increase when utilizing the hypothetical correction. The dose behind the cortical bone is also decreased as a consequence of the conservation of energy requirement. The opposite is true in the reverse conditions, i.e. when the "new/hypothetical" scaling factor is lower than the one calculated with the current used formula. This can be seen in Figure 24 in the air heterogeneity. As this is thought to be the desired effect to correct for the problems observed in ACE when a cortical bone heterogeneity is present, utilizing an effective scaling factor will likely work to account for an increased/decreased absorption ratio at the point of energy release to multiple-scattered photons. However, as earlier pointed out, the detailed design of such scaling factor is left to be derived in future work and it remains to be proven if an effective scaling factor will work in reality.

```python
def D_msc(rho, eta_msc, chi, iterations):
    """
    rho: List of densities at each position (iteration number x Delta_l)
    eta_msc: List of η_msc at each position
    chi: List of hypothetical correction of η_msc, χ_msc,  at each position
    iterations: Number of steps of size Delta_l taken
    """
    C0 = 1
    c0 = 1
    DeltaOmega = 1
    S2sc = 1
    Delta_l = 0.1 # cm
    R = 0
    c0b = 0
    l = 0
    lenght = []
    D = []
    for i in range(iterations):
        sigma = S2sc*rho[i]*DeltaOmega*(C0/c0)
        DeltaR = sigma*((1-np.exp(-(eta_msc[i]*chi[i]*c0*Delta_l)))/
                    ((eta_msc[i]*chi[i])*c0))
        c0b = ((c0b*R) + (c0*DeltaR))/(R+DeltaR)
        epsilon = np.exp(-(eta_msc[i]*chi[i])*c0b*Delta_l)
        D_ = (1/Delta_l)*(1/rho[i])*(((1-epsilon)*R) + (sigma*Delta_l -DeltaR))
        D.append(D_)
        l += Delta_l
        lenght.append(l)
        R = (R*epsilon) + DeltaR
    return lenght, D
```

Figure 22: The python script, written in python 3, to calculate D_C along the transport line in Figure 21, by iteration of the equations 43 to 48. *Chi* is either set to 1 at all locations or to $\frac{(\mu_{en}/\rho)_{med}}{(\mu_{en}/\rho)_{water}}$ in the case when the hypothetical correction factor in equation 50 is used.
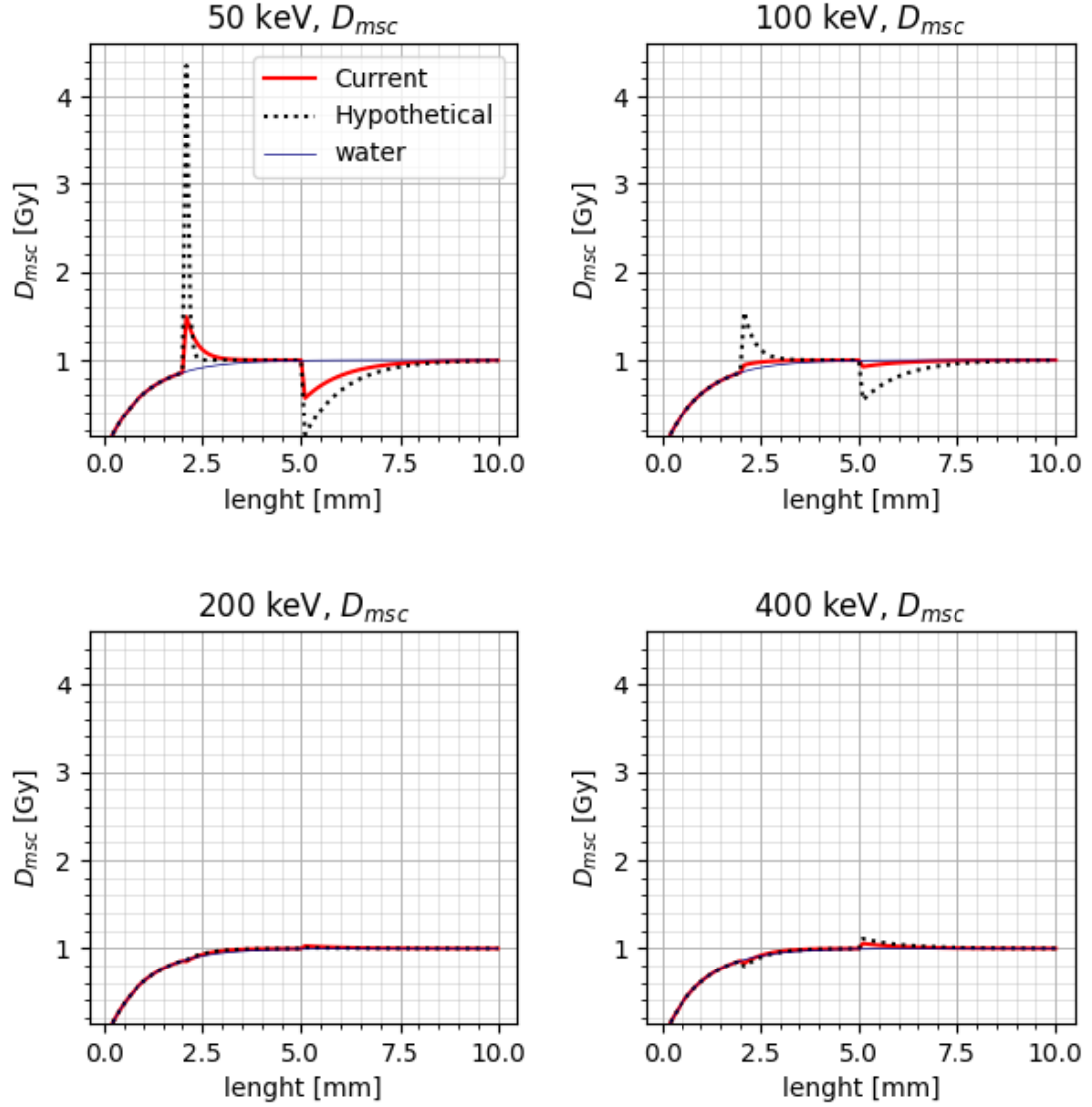
Figure 23: The multiple-scattered dose component $D_{\mathrm{msc},C}$ along a single transport line through voxels with a $S_{2\mathrm{sc}}$ value equal to 1 Gy. The multiple-scattered photon energy spectra is assumed to be monoenergetic and four different energies has been considered. A cortical bone heterogeneity is present in voxels located between 2-5 cm in on the transport line and all other voxels contain water. The dose along the transport line has been calculated with out the heterogeneity (blue solid lines), with the current attenuation scaling factor in equation 49 (red solid lines), and with the a hypothetical effective attenuation scaling factor in equation 50 (black dotted lines).
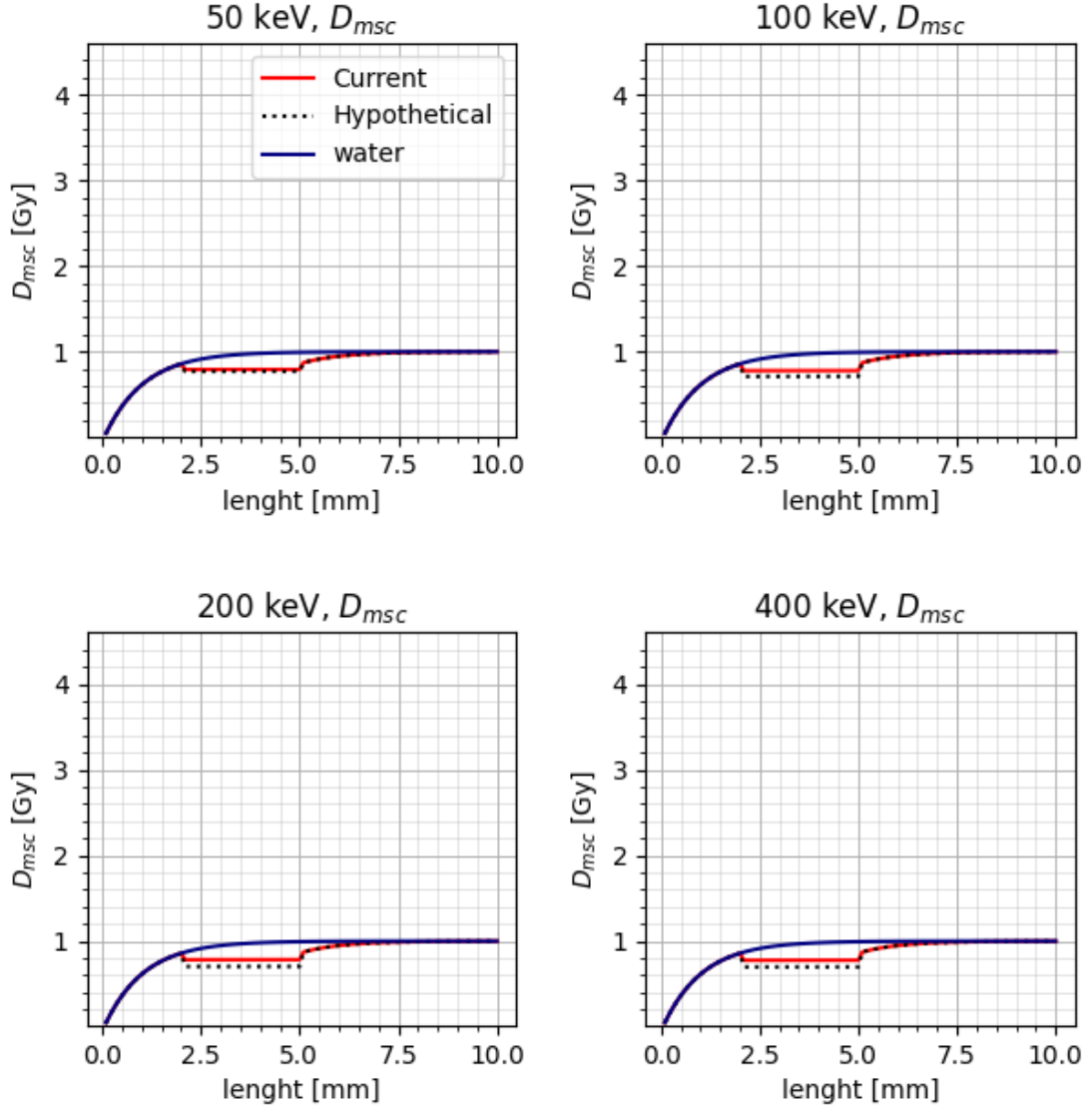
Figure 24: The multiple-scattered dose component $D_{\mathrm{msc},C}$ along a single transport line through voxels with a $S_{2\mathrm{sc}}$ value equal to 1 Gy. The multiple-scattered photon energy spectra is assumed to be monoenergetic and four different energies has been considered. An air heterogeneity is present in voxels located between 2-5 cm in on the transport line and all other voxels contain water. The dose along the transport line has been calculated with out the heterogeneity (blue solid lines), with the current attenuation scaling factor in equation 49 (red solid lines), and with the a hypothetical effective attenuation scaling factor in equation 50 (black dotted lines).